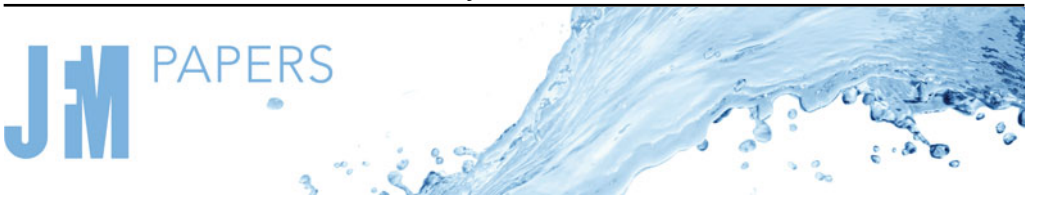
*J. Fluid Mech.* (2026), *vol.* 1029, A54, doi:10.1017/jfm.2026.11248



# Kinetic theory of binary fluid–surfactant systems: A variational framework

**Alexandra J. Hardy**[1], **Samuel Cameron**[1], **Steven McDonald**[1], **Abdallah Daddi-Moussa-Ider**[1] **and Elsen Tjhung**[1]

[1]School of Mathematics and Statistics, The Open University, Walton Hall, Kents Hill, Milton Keynes, MK7 6AA, UK

**Corresponding author:** Elsen Tjhung, elsen.tjhung@googlemail.com

(Received 15 July 2025; revised 4 December 2025; accepted 16 January 2026)

We derive a self-consistent hydrodynamic theory of coupled binary fluid–surfactant systems from the underlying microscopic physics using Rayleigh's variational principle. At the microscopic level, surfactant molecules are modelled as dumbbells that exert forces and torques on the fluid and interface while undergoing Brownian motion. We obtain the overdamped stochastic dynamics of these particles from a Rayleighian dissipation functional, which we then coarse-grain to derive a set of continuum equations governing the surfactant concentration, orientation, fluid density and velocity. This approach introduces a polarisation field $\boldsymbol{p}(\boldsymbol{r}, t)$, representing the average orientation of surfactants, which plays a central role in suppressing droplet coalescence. The remaining hydrodynamic equations are consistently obtained from a mesoscopic free energy functional. The resulting model accurately captures key surfactant phenomena, including surface tension reduction and droplet stabilisation, as confirmed by both perturbation theory and numerical simulations, and is thermodynamically consistent with both the Gibbs adsorption isotherm and Henry's law for adsorbed surfactant concentration.

**Key words:** variational methods, multiphase flow, kinetic theory

## 1. Introduction

Systems containing surfactants are widely studied due to their numerous industrial applications, including in medicine, cleaning products and the food industry (Tadros 2005; Shaban, Kang & Kim 2020. Their primary utility lies in their ability to adsorb at fluid–fluid interfaces, such as liquid–gas or oil–water boundaries, where they reduce surface tension and inhibit droplet coalescence (Mulqueen & Blankschtein 2002). For instance,

© The Author(s), 2026. Published by Cambridge University Press. This is an Open Access article, distributed under the terms of the Creative Commons Attribution licence (https://creativecommons.org/licenses/by/4.0/), which permits unrestricted re-use, distribution and reproduction, provided the original article is properly cited.



https://doi.org/10.1017/jfm.2026.11248 Published online by Cambridge University Press

in an emulsion of oil droplets dispersed in water, surfactants stabilise the droplet interfaces, thereby slowing the phase separation into two macroscopic oil and water phases. Surfactant molecules are amphiphilic, typically composed of a hydrophilic 'head' and a hydrophobic 'tail'. The hydrophilic head is attracted to the water phase, while the hydrophobic tail prefers the oil phase, leading to an orientation that is perpendicular to the interface (as shown in figure 1*a*). Upon adsorption at the interface, surfactants reduce the interfacial energy and thereby lower the surface tension. Once the interface becomes saturated, no further surfactant molecules can adsorb, causing the surface tension to level off (Touhami *et al.* 2001; Wang *et al.* 2017). Excess surfactants in the bulk phase may then self-assemble into micelles – spherical aggregates with hydrophobic tails hidden in the core and hydrophilic heads exposed to the surrounding fluid (Gangula, Suen & Conte 2010; Santos & Panagiotopoulos 2016). Beyond surface tension reduction, surfactants also suppress droplet coalescence (Dai & Leal 2008; Krebs, Schroën & Boom 2012), thereby enhancing the stability and mixing of otherwise immiscible phases.

Previous theoretical treatments of ternary systems – comprising two immiscible fluids and a surfactant population – have included Ising-like lattice models (Alexander 1978; Ahluwalia & Puri 1996), Potts models (Gilhøj *et al.* 1996) and direct molecular dynamics simulations (Laradji & Mouritsen 2000). Early continuum models either neglected the polarisation field entirely or integrated out its degrees of freedom from the dynamics (Kawasaki & Kawakatsu 1990; Anisimov *et al.* 1992). The first study to explicitly include the coarse-grained polarisation field dynamics (Melenkevitz & Javadpour 1997) neglected both hydrodynamic interactions and thermal fluctuations. More recent continuum models of surfactant-covered binary fluids employ a free energy functional that depends on the surfactant concentration but omits the explicit dynamics of the polarisation field $\boldsymbol{p}(\boldsymbol{r}, t)$. Instead of incorporating $\boldsymbol{p}(\boldsymbol{r}, t)$, such models introduce additional stabilising terms to prevent the surfactant from destabilising the diffuse interface (Liu & Zhang 2010; Zhu *et al.* 2020). These terms are often chosen to enforce Langmuir's adsorption isotherm (Kalam *et al.* 2021) and the Gibbs adsorption equation (Manikantan & Squires 2020), which respectively govern surfactant uptake at interfaces and the relationship between surface tension and surfactant concentration. As a result, these models can successfully capture the reduction in surface tension with increasing surfactant concentration (Liu & Zhang 2010). Coupling the surfactant and order parameter fields to the fluid velocity field further allows these models to reproduce, to some extent, the suppression of droplet coalescence (Liu & Zhang 2010; Soligo *et al.* 2019*a*,*b*).

A wide range of numerical methods have been employed to directly simulate the continuum equations of diffuse interface systems, including finite volume (Yamashita, Matsushita & Suekane 2024) and finite difference schemes (Teigen *et al.* 2011), as well as more specialised computational approaches (Booty & Siegel 2010; Yang 2021). Such simulations provide insights into the behaviour of surfactant-laden droplets under various conditions, including spinodal decomposition (Kim 2006), shear flows (Teigen *et al.* 2011) and wetting dynamics (Ganesan 2015). Alternative approaches to direct numerical simulation include lattice gas (Frisch, Hasslacher & Pomeau 1986) and lattice Boltzmann methods (Higuera, Succi & Benzi 1989; Benzi, Succi & Vergassola 1992), which were initially developed for binary fluid systems (Rothman & Keller 1988; Chan & Liang 1990) and later extended to ternary mixtures, where surfactants act as a third component (Theissen & Gompper 1999; Love *et al.* 2003; Kian Far *et al.* 2021). Lattice Boltzmann methods can be broadly classified as either free-energy-based methods or pseudopotential approaches (Krüger *et al.* 2017). The pseudopotential approach mimics attractive or repulsive interactions between different species of fluid molecules, but does not have a direct connection to microscopic physics. To date, only pseudopotential-based models



https://doi.org/10.1017/jfm.2026.11248 Published online by Cambridge University Press

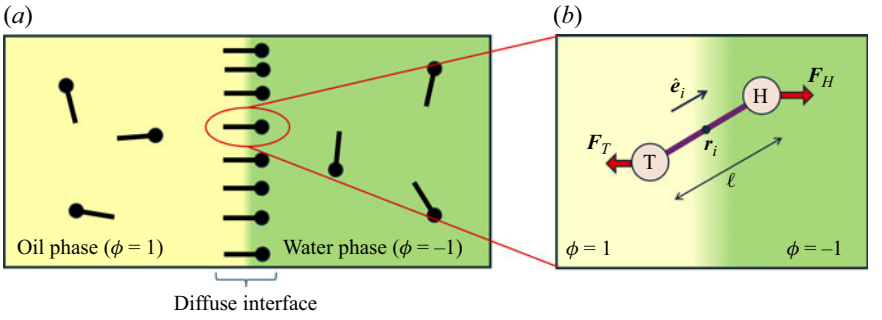



Figure 1. (*a*) is a schematic diagram illustrating how surfactants (black) are absorbed perpendicularly at the interface between two phases, e.g. water and oil phase (green and yellow, respectively). (*b*) shows a diagram showing the surfactant molecule modelled as a dumbbell, adsorbed into a diffuse water–oil interface, with 'head' H, 'tail' T, rod of length $\ell$, centre of mass $\boldsymbol{r}_i$ and orientation vector $\hat{\boldsymbol{e}}_i$, directed from 'tail' to 'head'. The fluid exerts a force on each mass point, $\boldsymbol{F}_H$ and $\boldsymbol{F}_T$, due to the hydrophilic/hydrophobic attraction between said mass points and the corresponding fluid phases. The binary fluid order parameter $\phi(\boldsymbol{r}, t)$ has values between 1 and $-1$ to represent the two fluid phases.

have been used to explicitly simulate the dynamics of the polarisation field associated with surfactant molecules – aside from Melenkevitz & Javadpour (1997), who neglected hydrodynamics.

In this work, we develop a continuum model of surfactant-laden binary fluids that is rigorously grounded in microscopic physics. Our central methodology is based on Rayleigh's minimum energy dissipation principle, which we use to derive the overdamped dynamics of surfactant molecules interacting with a diffuse interface. This variational approach allows us to self-consistently obtain both the stochastic microscopic dynamics and, upon coarse-graining, the macroscopic hydrodynamic equations for the coupled fields: binary fluid volume fraction $\phi(\boldsymbol{r}, t)$, surfactant concentration $c(\boldsymbol{r}, t)$, polarisation $\boldsymbol{p}(\boldsymbol{r}, t)$ and fluid velocity $\boldsymbol{v}(\boldsymbol{r}, t)$. Unlike many previous models that introduce phenomenological terms to enforce stability or empirical adsorption laws, our formulation derives all equations from a single Rayleighian functional and a unified coarse-grained free energy, preserving detailed balance at equilibrium and ensuring thermodynamic consistency.

A key advantage of this framework is that Marangoni flows arise naturally without the need to impose an additional surface-tension–gradient term. Because each surfactant exerts a tangential force on the interface, any spatial heterogeneity in surfactant concentration produces an excess stress that drives flow along the interface. The resulting long-ranged disturbances in the fluid velocity are therefore the exact analogue of the classical Marangoni flows generated by gradients in surface tension. Moreover, the model is thermodynamically consistent with both the Gibbs adsorption isotherm for surface-tension reduction and Henry's law for the excess of surfactant at interfaces.

Assuming weak coupling between the fluid and surfactants allows us to obtain a perturbative equilibrium solution for a flat interface. We validate this analytical solution by numerically simulating the same planar interface using a hybrid finite-difference–pseudospectral method. This solution confirms that our model accurately captures the reduction in surface tension due to surfactant adsorption, in agreement with both previous phase-field models and experimental observations. We then perform numerical simulations of an emulsion to demonstrate how the inclusion of the polarisation field $\boldsymbol{p}(\boldsymbol{r}, t)$ suppresses droplet coalescence. Previous studies have used pseudopotential-based methods to generate ultra-stable emulsions (Pelusi *et al.* 2022). In contrast, our results



https://doi.org/10.1017/jfm.2026.11248 Published online by Cambridge University Press

show that stable emulsification can be achieved within a continuum framework, provided the surfactant polarisation dynamics is explicitly incorporated.

## 2. Microscopic derivation of the hydrodynamic equations

At the microscopic level, each surfactant molecule is modelled as a dumbbell composed of two mass points: a hydrophilic head (H) and a hydrophobic tail (T), connected by a rigid rod of length $\ell$ (Kawakatsu & Kawasaki 1990), see figure 1*b*. The surrounding fluid is treated as a continuum, described by a velocity field $\boldsymbol{v}(\boldsymbol{r}, t)$ and a volume fraction field $\phi(\boldsymbol{r}, t)$. The field $\phi(\boldsymbol{r}, t)$ represents the local volume fraction of one component (e.g. oil) relative to the total volume of both components (oil and water), with $\phi > 0$ indicating a local excess of component 1 and $\phi < 0$ indicating a local excess of component 2. In this work, we take component 1 to be oil and component 2 to be water, although this labelling is arbitrary. Under appropriate conditions, a diffuse oil–water interface emerges, to which the surfactant molecules are attracted. In figure 1*b*, the vector $\hat{\boldsymbol{e}}_i$ denotes the orientation of surfactant molecule $i$, pointing from tail to head, with the centre of mass located at $\boldsymbol{r}_i$. The head is attracted to the aqueous phase, while the tail prefers the oil phase. These preferential interactions generate a net force $\boldsymbol{F}_i^{fluid}$ and a net torque $\boldsymbol{T}_i^{fluid}$ (about the centre of mass) when the molecule is not perpendicular with the interface or displaced from the midpoint of the interface. From figure 1*b*, $\boldsymbol{F}_i^{fluid}$ and $\boldsymbol{T}_i^{fluid}$ can be expressed as

$$\boldsymbol{F}_i^{fluid} = \boldsymbol{F}_H(\boldsymbol{r}_i^+) + \boldsymbol{F}_T(\boldsymbol{r}_i^-), \tag{2.1a}$$

$$\boldsymbol{T}_i^{fluid} = \frac{\ell}{2}\,\hat{\boldsymbol{e}}_i \times \boldsymbol{F}_H(\boldsymbol{r}_i^+) - \frac{\ell}{2}\,\hat{\boldsymbol{e}}_i \times \boldsymbol{F}_T(\boldsymbol{r}_i^-), \tag{2.1b}$$

where $\boldsymbol{F}_H(\boldsymbol{r}_i^+)$ and $\boldsymbol{F}_T(\boldsymbol{r}_i^-)$ are the forces acting from the fluid on the surfactant mass points H and T, respectively, with $\boldsymbol{r}_i^\pm = \boldsymbol{r}_i \pm \ell\hat{\boldsymbol{e}}_i/2$ denoting the positions of H (for $+$) and T (for $-$). The forces are obtained as

$$\boldsymbol{F}_H(\boldsymbol{r}_i^+) = -\chi\nabla\phi(\boldsymbol{r})|_{\boldsymbol{r}=\boldsymbol{r}_i^+}, \tag{2.2a}$$

$$\boldsymbol{F}_T(\boldsymbol{r}_i^-) = +\chi\nabla\phi(\boldsymbol{r})|_{\boldsymbol{r}=\boldsymbol{r}_i^-}, \tag{2.2b}$$

where $\nabla\phi(\boldsymbol{r})|_{\boldsymbol{r}=\boldsymbol{r}_i^\pm}$ is the spatial derivative of $\phi(\boldsymbol{r})$, evaluated at $\boldsymbol{r}_i^\pm$. In addition, $\chi > 0$ is the interaction strength between each mass point and their preferential fluid phases (assumed to be equal in magnitude). Substituting (2.2) into (2.1), and Taylor expanding for small $\ell$, we obtain the net force and the net torque acting on each molecule $i$ from the fluid:

$$\boldsymbol{F}_i^{fluid} = -\chi\ell(\hat{\boldsymbol{e}}_i\cdot\nabla_i)\nabla_i\phi(\boldsymbol{r}_i) + \mathcal{O}(\ell^2), \tag{2.3a}$$

$$\boldsymbol{T}_i^{fluid} = -\chi\ell\hat{\boldsymbol{e}}_i \times \nabla_i\phi(\boldsymbol{r}_i) + \mathcal{O}(\ell^2), \tag{2.3b}$$

where $\nabla_i$ indicates derivative with respect to $\boldsymbol{r}_i$, the centre of mass of molecule $i$. Motivated by the structure of the above-mentioned force and torque expressions, we derive the corresponding microscopic dynamics. From this microcopic dynamics, we can then obtain the coarse-grained hydrodynamic equations governing the coupled surfactant–binary fluid systems.



https://doi.org/10.1017/jfm.2026.11248 Published online by Cambridge University Press

### 2.1. *Rayleighian dissipation for a single surfactant molecule in a binary fluid*

In this section, we first derive the microscopic dynamics of a single surfactant molecule in a binary fluid using Rayleigh's minimum energy dissipation principle (Doi 2011, 2013). We then extend this framework to an ensemble of non-interacting surfactant molecules by introducing a single-particle distribution function. This allows us to derive the coarse-grained hydrodynamic equations in terms of the concentration field $c(\boldsymbol{r}, t)$, polarisation field $\boldsymbol{p}(\boldsymbol{r}, t)$, binary fluid volume fraction field $\phi(\boldsymbol{r}, t)$ and velocity field $\boldsymbol{v}(\boldsymbol{r}, t)$.

We first consider a system of a single dumbbell with two point masses at $\boldsymbol{r}^+$ and $\boldsymbol{r}^-$, representing the positions of the head and the tail, respectively. We also have $|\boldsymbol{r}^+ - \boldsymbol{r}^-| = \ell$, where $\ell$ is the length of the dumbbell. The free energy of a single dumbbell particle in a continuum fluid is then given by

$$A[\phi, \{\boldsymbol{r}^+, \boldsymbol{r}^-\}] = F_{fluid}[\phi] + \int d^d r \, \left\{\chi \left[\delta(\boldsymbol{r} - \boldsymbol{r}^+) - \delta(\boldsymbol{r} - \boldsymbol{r}^-)\right] \phi(\boldsymbol{r})\right\}, \tag{2.4}$$

where

$$F_{fluid}[\phi] = \int d^d r \left\{\frac{\alpha}{2}\phi^2 + \frac{\beta}{4}\phi^4 + \frac{\kappa}{2}|\nabla\phi|^2\right\} \tag{2.5}$$

is a typical free energy of a binary fluid, containing a double-well potential (for $\alpha < 0$ and $\beta > 0$) to drive bulk phase separation which competes with a squared-gradient term to penalise surface proliferation. Here, we take $\alpha = -\beta < 0$, so that equilibrium phases correspond to $\phi = \pm\sqrt{-\alpha/\beta} = \pm 1$. Note that $d$ is the spatial dimension and the integral is taken over the volume of the system. The second term in (2.4) couples the two discrete head and tail positions to the volume fraction field, with each particle–field interaction characterised by an interaction strength $\chi$ (Hardy, Daddi-Moussa-Ider & Tjhung 2024). We now introduce the orientation unit vector $\hat{\boldsymbol{e}}$ and the centre of mass position $\boldsymbol{R}$ to be

$$\hat{\boldsymbol{e}} = \frac{\boldsymbol{r}^+ - \boldsymbol{r}^-}{\ell} \quad \text{and} \quad \boldsymbol{R} = \frac{\boldsymbol{r}^+ + \boldsymbol{r}^-}{2}. \tag{2.6}$$

Then, (2.4) becomes

$$A[\phi, \{\boldsymbol{R}, \hat{\boldsymbol{e}}\}] = F_{fluid}[\phi] + \int d^d r \left\{\chi \left[\delta\left(\boldsymbol{r} - \left(\boldsymbol{R} + \frac{\ell}{2}\hat{\boldsymbol{e}}\right)\right) - \delta\left(\boldsymbol{r} - \left(\boldsymbol{R} - \frac{\ell}{2}\hat{\boldsymbol{e}}\right)\right)\right] \phi(\boldsymbol{r})\right\}. \tag{2.7}$$

Taylor expanding (2.7) for small $\ell$, we may obtain

$$A[\phi, \{\boldsymbol{R}, \hat{\boldsymbol{e}}\}] = F_{fluid}[\phi] + \chi\ell(\hat{\boldsymbol{e}} \cdot \nabla_{\boldsymbol{R}})\phi(\boldsymbol{R}) + \mathcal{O}(\ell^3), \tag{2.8}$$

where $\nabla_{\boldsymbol{R}}$ denotes spatial derivative with respect to the centre of mass of the dumbbell $\boldsymbol{R}$. Thus, the hybrid discrete-particle–continuum-fluid free energy is a functional of the volume fraction field $\phi(\boldsymbol{r})$ and a function of discrete variables $\boldsymbol{R}$ and $\hat{\boldsymbol{e}}$. Ultimately, we aim to re-cast (2.7) or (2.8) as a purely continuum free energy.

Following Doi (2011), we next write down the Rayleigh dissipation functional

$$\mathcal{R}[\partial_t\phi, \boldsymbol{v}_1, \boldsymbol{v}_2, \{\dot{\boldsymbol{r}}^+, \dot{\boldsymbol{r}}^-\}] = \Phi_1[\boldsymbol{v}] + \Phi_2[\boldsymbol{v}_1, \boldsymbol{v}_2] + \Phi_3[\boldsymbol{v}, \{\dot{\boldsymbol{r}}^+, \dot{\boldsymbol{r}}^-\}] + \dot{A}, \tag{2.9}$$

which is a functional of the rate of change of the volume fraction $\partial_t\phi$; the velocity of fluid component 1, $\boldsymbol{v}_1(\boldsymbol{r}, t)$; the velocity of fluid component 2, $\boldsymbol{v}_2(\boldsymbol{r}, t)$; and the velocities of the discrete particles $\{\dot{\boldsymbol{r}}^+, \dot{\boldsymbol{r}}^-\}$. We may also further define the total velocity of the fluid to be

https://doi.org/10.1017/jfm.2026.11248 Published online by Cambridge University Press

$$\boldsymbol{v}(\boldsymbol{r},t)=\frac{1+\phi}{2}\boldsymbol{v}_1(\boldsymbol{r},t)+\frac{1-\phi}{2}\boldsymbol{v}_2(\boldsymbol{r},t), \tag{2.10}$$

so that either $\boldsymbol{v}_1$ or $\boldsymbol{v}_2$ may be expressed in terms of $\boldsymbol{v}$ and the other. We use a dot over any variable to denote its total time-derivative. We neglect the volume of discrete particles in this formulation. The first dissipation term in (2.9) denotes the viscous dissipation of the incompressible Newtonian fluid,

$$\Phi_1[\boldsymbol{v}]=\int d^dr\,\frac{\eta}{4}\left[\nabla\boldsymbol{v}+(\nabla\boldsymbol{v})^T\right]^2-\int d^dr\,P(\boldsymbol{r})\nabla\cdot\boldsymbol{v}, \tag{2.11}$$

where $\eta$ is the fluid viscosity (assumed to be the same for both components of the fluid) and $P(\boldsymbol{r})$ is a Lagrange multiplier to enforce incompressibility condition $\nabla\cdot\boldsymbol{v}=0$, which also happens to be the pressure of the fluid. The second dissipation term in (2.9) represents dissipation due to velocity differences between the two fluid components,

$$\Phi_2[\boldsymbol{v}_1,\boldsymbol{v}_2]=\int d^dr\,\frac{\xi}{2}(\boldsymbol{v}_1-\boldsymbol{v}_2)^2=\int d^dr\,\frac{2\xi}{(1-\phi)^2}(\boldsymbol{v}_1-\boldsymbol{v})^2, \tag{2.12}$$

where $\xi>0$ is a phenomenological dissipation parameter related to the mobility. The third term in (2.9) couples the fluid velocity to the particle velocities

$$\Phi_3[\boldsymbol{v},\{\dot{\boldsymbol{r}}^+,\dot{\boldsymbol{r}}^-\}]=-\int d^dr\left\{\delta(\boldsymbol{r}-\boldsymbol{r}^+)\boldsymbol{f}^+\cdot(\boldsymbol{v}(\boldsymbol{r})-\dot{\boldsymbol{r}}^+)+\delta(\boldsymbol{r}-\boldsymbol{r}^-)\boldsymbol{f}^-\cdot(\boldsymbol{v}(\boldsymbol{r})-\dot{\boldsymbol{r}}^-)\right\}, \tag{2.13}$$

where $\boldsymbol{f}^\pm$ are constraint forces which enforce $\boldsymbol{v}(\boldsymbol{r}^\pm)=\dot{\boldsymbol{r}}^\pm$ (similar to Lagrange multipliers). This is equivalent to introducing point forces acting on the fluid (i.e. Stokeslet solution). We can define the angular velocity of the dumbbell $\boldsymbol{\omega}$ to be $\dot{\hat{\boldsymbol{e}}}=\boldsymbol{\omega}\times\hat{\boldsymbol{e}}$. The rate of change of the positions $\dot{\boldsymbol{r}}^\pm$ can then be written in terms of $\dot{\boldsymbol{R}}$ and $\boldsymbol{\omega}$:

$$\dot{\boldsymbol{r}}^\pm=\dot{\boldsymbol{R}}\pm\boldsymbol{\omega}\times\frac{\ell}{2}\hat{\boldsymbol{e}}. \tag{2.14}$$

Using (2.14), (2.13) can then be written in terms of $\dot{\boldsymbol{R}}$ and $\boldsymbol{\omega}$, and thus, $\Phi_3[\boldsymbol{v},\{\dot{\boldsymbol{R}},\boldsymbol{\omega}\}]$ is now a function of $\dot{\boldsymbol{R}}$ and $\boldsymbol{\omega}$. The final term in (2.9) is simply the derivative of the free energy with time,

$$\begin{aligned}\dot{A}[\partial_t\phi,\{\dot{\boldsymbol{R}},\boldsymbol{\omega}\}] \;=\;& \int d^dr\left\{\frac{\delta F_{fluid}}{\delta\phi}\partial_t\phi\right\}\\ &+\int d^dr\left\{\chi\,\partial_t\phi\left[\delta\left(\boldsymbol{r}-\left(\boldsymbol{R}+\frac{\ell}{2}\hat{\boldsymbol{e}}\right)\right)-\delta\left(\boldsymbol{r}-\left(\boldsymbol{R}-\frac{\ell}{2}\hat{\boldsymbol{e}}\right)\right)\right]\right\}\\ &+\chi\left[\nabla\phi(\boldsymbol{r})|_{\boldsymbol{r}=\boldsymbol{R}+\ell\hat{\boldsymbol{e}}/2}-\nabla\phi(\boldsymbol{r})|_{\boldsymbol{r}=\boldsymbol{R}-\ell\hat{\boldsymbol{e}}/2}\right]\cdot\dot{\boldsymbol{R}}\\ &+\frac{\ell\chi}{2}\left[\nabla\phi(\boldsymbol{r})|_{\boldsymbol{r}=\boldsymbol{R}+\ell\hat{\boldsymbol{e}}/2}+\nabla\phi(\boldsymbol{r})|_{\boldsymbol{r}=\boldsymbol{R}-\ell\hat{\boldsymbol{e}}/2}\right]\cdot\boldsymbol{\omega}\times\hat{\boldsymbol{e}},\end{aligned} \tag{2.15}$$

where we have expressed $\dot{\hat{\boldsymbol{e}}}=\boldsymbol{\omega}\times\hat{\boldsymbol{e}}$. Minimising the Rayleighian $\mathcal{R}[\partial_t\phi,\boldsymbol{v},\boldsymbol{v}_1,\{\dot{\boldsymbol{R}},\boldsymbol{\omega}\}]$ with respect to the generalised velocities $\partial_t\phi$, $\boldsymbol{v}$, $\boldsymbol{v}_1$, $\dot{\boldsymbol{R}}$ and $\boldsymbol{\omega}$, and subject to the constraint that volume fraction is conserved, i.e.

$$\partial_t\phi+\nabla\cdot[(1+\phi)\boldsymbol{v}_1]=0, \tag{2.16}$$



https://doi.org/10.1017/jfm.2026.11248 Published online by Cambridge University Press

we get the equations of motion for the system:

$$\partial_t \phi = -\boldsymbol{v}\cdot\nabla\phi + M\nabla^2\left(\frac{\delta A}{\delta\phi}\right), \tag{2.17a}$$

$$\begin{aligned}\boldsymbol{v}(\boldsymbol{r}) = &\int d^d r' \left[\boldsymbol{O}(\boldsymbol{r}-\boldsymbol{r}')\cdot\left(-\phi(\boldsymbol{r}')\nabla'\frac{\delta A}{\delta\phi(\boldsymbol{r}')}\right)\right] \\ &+ \left[\boldsymbol{O}(\boldsymbol{r}-\boldsymbol{R}) + \frac{\ell^2}{8}(\hat{\boldsymbol{e}}\hat{\boldsymbol{e}} : \nabla_{\boldsymbol{R}}\nabla_{\boldsymbol{R}})\boldsymbol{O}(\boldsymbol{r}-\boldsymbol{R})\right]\cdot\boldsymbol{g} \\ &+ \left[(\boldsymbol{e}\cdot\nabla_{\boldsymbol{R}})\boldsymbol{O}(\boldsymbol{r}-\boldsymbol{R}) + \frac{\ell^2}{3!}(\hat{\boldsymbol{e}}\hat{\boldsymbol{e}}\hat{\boldsymbol{e}} : \nabla_{\boldsymbol{R}}\nabla_{\boldsymbol{R}}\nabla_{\boldsymbol{R}})\boldsymbol{O}(\boldsymbol{r}-\boldsymbol{R})\right]\cdot\boldsymbol{h} + \mathcal{O}(\ell^3)\end{aligned} \tag{2.17b}$$

$$\boldsymbol{g} = -\ell\chi(\hat{\boldsymbol{e}}\cdot\nabla_{\boldsymbol{R}})\nabla_{\boldsymbol{R}}\phi(\boldsymbol{R}) + \mathcal{O}(\ell^3), \tag{2.17c}$$

$$\boldsymbol{h} = -\ell\chi\nabla_{\boldsymbol{R}}\phi(\boldsymbol{R}) + \mathcal{O}(\ell^3), \tag{2.17d}$$

$$\dot{\boldsymbol{R}} = \boldsymbol{v}(\boldsymbol{R}) + \mathcal{O}(\ell^2), \tag{2.17e}$$

$$\dot{\hat{\boldsymbol{e}}} = (\hat{\boldsymbol{e}}\cdot\nabla_{\boldsymbol{R}})\boldsymbol{v}(\boldsymbol{R}) + \mathcal{O}(\ell^2), \tag{2.17f}$$

where we have defined $\boldsymbol{g} = \boldsymbol{f}_2 + \boldsymbol{f}_1$ and $\boldsymbol{h} = \ell(\boldsymbol{f}_2 - \boldsymbol{f}_1)/2$. Here, $\boldsymbol{O}(\boldsymbol{r})$ is the second rank Oseen tensor, which in three dimensions ($d = 3$), is given by

$$\boldsymbol{O}(\boldsymbol{r}) = \frac{1}{8\pi\eta r}\left(\boldsymbol{I} + \frac{\boldsymbol{r}\boldsymbol{r}}{r^2}\right), \tag{2.18}$$

where $\boldsymbol{I}$ is the identity matrix. To obtain (2.17), we have assumed that the binary fluid dissipation coefficient, $\xi \equiv (1+\phi)^2(1-\phi)^2/(4M)$, depends explicitly on the volume fraction, so that the mobility $M$ in (2.17*a*) remains constant.

The singular nature of $\boldsymbol{O}(\boldsymbol{r})$ at $\boldsymbol{r} = \boldsymbol{0}$ poses a problem, as the centre-of-mass and orientation dynamics both require evaluating $\boldsymbol{v}(\boldsymbol{R})$. However, there is a precedent in the literature to remedy this, particularly in polymer physics when one deals with strings of spherical beads (Doi & Edwards 1986). One can begin by assuming the singular term in the velocity dynamics is omitted. We will denote the remaining external flow velocity as $\boldsymbol{v}_{ext}(\boldsymbol{r})$, defined simply as

$$\boldsymbol{v}_{ext}(\boldsymbol{r}) = \int d^d r' \left[\boldsymbol{O}(\boldsymbol{r}-\boldsymbol{r}')\cdot\left(-\phi(\boldsymbol{r}')\nabla'\frac{\delta A}{\delta\phi(\boldsymbol{r}')}\right)\right] + \mathcal{O}(\ell^3). \tag{2.19}$$

To compensate for the neglect of the singular self-interaction flow, one needs to supplement the equations of $\dot{\boldsymbol{R}}$ and $\dot{\hat{\boldsymbol{e}}}$ by a self-interaction term, which is taken *ad hoc* to be the mobility matrix of the isolated particle multiplied by the force on that particle (neglecting hydrodynamic forces). For us, we choose the mobility matrix which is consistent with an isolated needle-like particle, as that is the closest to our dipolar case for which an exact solution is available. Then,

$$\dot{\hat{\boldsymbol{e}}} = \left(\boldsymbol{I} - \hat{\boldsymbol{e}}\hat{\boldsymbol{e}}\right)\cdot\left[(\hat{\boldsymbol{e}}\cdot\nabla_{\boldsymbol{R}})\boldsymbol{v}_{ext}(\boldsymbol{R}) - \frac{1}{\gamma_r}\frac{\partial A}{\partial\hat{\boldsymbol{e}}}\right], \tag{2.20a}$$

$$\dot{\boldsymbol{R}} = \boldsymbol{v}_{ext}(\boldsymbol{R}) - \left[\frac{1}{\zeta_\parallel}\hat{\boldsymbol{e}}\hat{\boldsymbol{e}} + \frac{1}{\zeta_\perp}\left(\boldsymbol{I} - \hat{\boldsymbol{e}}\hat{\boldsymbol{e}}\right)\right]\cdot\frac{\partial A}{\partial\boldsymbol{R}}. \tag{2.20b}$$



https://doi.org/10.1017/jfm.2026.11248 Published online by Cambridge University Press

The operator $(\boldsymbol{I}-\hat{\boldsymbol{e}}\hat{\boldsymbol{e}})$ is known as the perpendicular projection operator, as it projects any vector $\boldsymbol{V}$ onto the plane perpendicular to $\hat{\boldsymbol{e}}$, i.e. $(\boldsymbol{I}-\hat{\boldsymbol{e}}\hat{\boldsymbol{e}})\cdot\boldsymbol{V}$. We employ this operator in (2.20*a*) to ensure that the unit-length constraint $|\hat{\boldsymbol{e}}|=1$ is maintained throughout the dynamics. In (2.20), $\gamma_r$ is the rotational friction, and $\zeta_\parallel$ and $\zeta_\perp$ are the translational friction parallel and perpendicular to $\hat{\boldsymbol{e}}$, respectively. In the case of ellipsoidal particles, these friction coefficients can be written in terms of microscopic parameters (Kim & Karrila 2005); Hoffmann *et al.* 2009). This result reproduces the Jeffrey orbits if we define the symmetric and anti-symmetric tensors

$$(\boldsymbol{D}_{ext})_{\alpha\beta}\equiv\frac{1}{2}\left[(\nabla)_\alpha(\boldsymbol{v}_{ext})_\beta+(\nabla)_\beta(\boldsymbol{v}_{ext})_\alpha\right], \tag{2.21a}$$

$$(\boldsymbol{\Omega}_{ext})_{\alpha\beta}\equiv\frac{1}{2}\left[(\nabla)_\alpha(\boldsymbol{v}_{ext})_\beta-(\nabla)_\beta(\boldsymbol{v}_{ext})_\alpha\right], \tag{2.21b}$$

i.e.

$$\dot{\hat{\boldsymbol{e}}}=\underbrace{-\boldsymbol{\Omega}_{ext}(\boldsymbol{R})\cdot\hat{\boldsymbol{e}}+B\left[\boldsymbol{D}_{ext}(\boldsymbol{R})\cdot\hat{\boldsymbol{e}}-\left(\hat{\boldsymbol{e}}\cdot\boldsymbol{D}_{ext}(\boldsymbol{R})\cdot\hat{\boldsymbol{e}}\right)\hat{\boldsymbol{e}}\right]}_{(\boldsymbol{I}-\hat{\boldsymbol{e}}\hat{\boldsymbol{e}})\cdot(\hat{\boldsymbol{e}}\cdot\nabla_{\boldsymbol{R}})\boldsymbol{v}_{ext}(\boldsymbol{R})\text{ for }B=1}-\left(\boldsymbol{I}-\hat{\boldsymbol{e}}\hat{\boldsymbol{e}}\right)\cdot\left(\frac{1}{\gamma_r}\frac{\partial A}{\partial\hat{\boldsymbol{e}}}\right), \tag{2.22}$$

though we specifically have $B=1$ since we assumed the surfactant had a needle-like aspect ratio in our derivation. In the case of ellipsoidal particles, $B$ is related to the aspect ratio of the particle $\Delta$ via $B=(\Delta^2-1)/(\Delta^2+1)$ (Jeffery 1922). Up to this point, we have derived the dynamics of a single surfactant molecule in the presence of a phase-separating binary fluid, (2.20*a*), (2.20*b*) and (2.22), subject to external flow due to phase separation, (2.19).

Finally, we introduce noise to the single particle dynamics to get the Ito stochastic differential equations (in $d$ dimension),

$$\begin{aligned}d\boldsymbol{R}=&\left\{\boldsymbol{v}_{ext}(\boldsymbol{R})-\left[\frac{1}{\zeta_\parallel}\hat{\boldsymbol{e}}\hat{\boldsymbol{e}}+\frac{1}{\zeta_\perp}\left(\boldsymbol{I}-\hat{\boldsymbol{e}}\hat{\boldsymbol{e}}\right)\right]\cdot\frac{\partial A}{\partial\boldsymbol{R}}\right\}\,\mathrm{d}t\\&+\left[\sqrt{\frac{2k_BT}{\zeta_\parallel}}\hat{\boldsymbol{e}}\hat{\boldsymbol{e}}+\sqrt{\frac{2k_BT}{\zeta_\perp}}\left(\boldsymbol{I}-\hat{\boldsymbol{e}}\hat{\boldsymbol{e}}\right)\right]\cdot\mathrm{d}\boldsymbol{W}_{\boldsymbol{R}},\end{aligned} \tag{2.23a}$$

$$d\hat{\boldsymbol{e}}=\left(\boldsymbol{I}-\hat{\boldsymbol{e}}\hat{\boldsymbol{e}}\right)\cdot\left\{\left[(\hat{\boldsymbol{e}}\cdot\nabla_{\boldsymbol{R}})\boldsymbol{v}_{ext}(\boldsymbol{R})-\frac{1}{\gamma_r}\frac{\partial A}{\partial\hat{\boldsymbol{e}}}\right]\mathrm{d}t+\sqrt{\frac{2k_BT}{\gamma_r}}\,\mathrm{d}\boldsymbol{W}_{\boldsymbol{e}}\right\}-\frac{(d-1)k_BT}{\gamma_r}\hat{\boldsymbol{e}}\,\mathrm{d}t, \tag{2.23b}$$

where $\mathrm{d}\boldsymbol{W}_{\boldsymbol{R}}$ and $\mathrm{d}\boldsymbol{W}_{\boldsymbol{e}}$ are Gaussian white noise with zero mean and variance $\mathrm{d}t$. If one instead wanted the Stratonovich form of the equations, the last term (i.e. the drift) is omitted in (2.23*b*). Using the form of the free energy $A[\phi,\{\boldsymbol{R},\hat{\boldsymbol{e}}\}]$ in (2.8), we can calculate (up to order $\ell^2$)

$$\frac{\partial A}{\partial\boldsymbol{R}}=\chi\ell(\hat{\boldsymbol{e}}\cdot\nabla_{\boldsymbol{R}})\nabla_{\boldsymbol{R}}\phi(\boldsymbol{R})=-\boldsymbol{F}^{fluid}, \tag{2.24a}$$

$$\frac{\partial A}{\partial\hat{\boldsymbol{e}}}=\chi\ell\nabla_{\boldsymbol{R}}\phi(\boldsymbol{R})=\underbrace{\chi\ell\left[\hat{\boldsymbol{e}}\times\nabla_{\boldsymbol{R}}\phi(\boldsymbol{R})\right]}_{-\boldsymbol{T}^{fluid}}\times\hat{\boldsymbol{e}}+\chi\ell\left[\hat{\boldsymbol{e}}\cdot\nabla_{\boldsymbol{R}}\phi(\boldsymbol{R})\right]\hat{\boldsymbol{e}}. \tag{2.24b}$$



https://doi.org/10.1017/jfm.2026.11248 Published online by Cambridge University Press

Note that the last term in (2.24*b*) does not affect the dynamics due to the perpendicular projection operator $\boldsymbol{I}-\hat{\boldsymbol{e}}\hat{\boldsymbol{e}}$ in (2.23*b*). Thus, we identify the derivatives $\partial A/\partial \boldsymbol{R}$ and $\partial A/\partial \hat{\boldsymbol{e}}$ as being directly related to the net force $\boldsymbol{F}^{fluid}$ and net torque $\boldsymbol{T}^{fluid}$ exerted by the fluid on the molecule (cf. (2.3)). Accordingly, the deterministic parts of (2.23) in the absence of external flow become

$$\frac{\mathrm{d}\boldsymbol{R}}{\mathrm{d}t}=\left[\frac{1}{\zeta_{\parallel}}\hat{\boldsymbol{e}}\hat{\boldsymbol{e}}+\frac{1}{\zeta_{\perp}}\left(\boldsymbol{I}-\hat{\boldsymbol{e}}\hat{\boldsymbol{e}}\right)\right]\cdot\boldsymbol{F}^{fluid}, \tag{2.25a}$$

$$\frac{\mathrm{d}\hat{\boldsymbol{e}}}{\mathrm{d}t}=\frac{1}{\gamma_r}\boldsymbol{T}^{fluid}\times\hat{\boldsymbol{e}}, \tag{2.25b}$$

as expected from overdamped dynamics.

### 2.2. *Coarse-graining the single surfactant particle dynamics*

The dynamics described in (2.23*a*) and (2.23*b*) in terms of surfactant particle position $\boldsymbol{R}$ and orientation $\hat{\boldsymbol{e}}$ can be equivalently described by the Smoluchowski equation (Doi & Edwards 1986; Doi 2011):

$$\frac{\partial\psi}{\partial t}=-\boldsymbol{\nabla}\cdot\boldsymbol{J}_{\boldsymbol{r}}+\boldsymbol{\mathcal{R}}\cdot\left(\frac{k_BT}{\gamma_r}\boldsymbol{\mathcal{R}}\psi+\frac{1}{\gamma_r}\psi\boldsymbol{\mathcal{R}}A-\hat{\boldsymbol{e}}\times\boldsymbol{K}\cdot\hat{\boldsymbol{e}}\psi\right), \tag{2.26}$$

where $\psi(\boldsymbol{r},\hat{\boldsymbol{e}},t)$ is the probability density for the surfactant particle. More precisely, $\psi(\boldsymbol{r},\hat{\boldsymbol{e}},t)d^dr d^{d-1}\hat{e}$ is the probability of finding a surfactant particle inside an infinitesimal volume $d^dr$, located at $\boldsymbol{r}$, with the orientation pointing in the direction of the solid angle $d^{d-1}\hat{e}$, located at $\hat{\boldsymbol{e}}$. In (2.26), $\boldsymbol{K}$ is defined to be $\boldsymbol{K}\equiv(\boldsymbol{\nabla}\boldsymbol{v}_{ext})^T$ or $(\boldsymbol{K})_{\alpha\beta}\equiv(\boldsymbol{\nabla})_\beta(\boldsymbol{v}_{ext})_\alpha$. We have also define the angular derivative operator $\boldsymbol{\mathcal{R}}$ to be

$$(\boldsymbol{\mathcal{R}})_\alpha\equiv\left(\hat{\boldsymbol{e}}\times\frac{\partial}{\partial\hat{\boldsymbol{e}}}\right)_\alpha=\varepsilon_{\alpha\beta\gamma}(\hat{\boldsymbol{e}})_\beta\left(\frac{\partial}{\partial\hat{\boldsymbol{e}}}\right)_\gamma. \tag{2.27}$$

Here, $\boldsymbol{J}_{\boldsymbol{r}}$ in (2.26) is the positional flux,

$$\boldsymbol{J}_{\boldsymbol{r}}\equiv\left\{\boldsymbol{v}_{ext}(\boldsymbol{r})-\left[\frac{1}{\zeta_{\parallel}}\hat{\boldsymbol{e}}\hat{\boldsymbol{e}}+\frac{1}{\zeta_{\perp}}\left(\boldsymbol{I}-\hat{\boldsymbol{e}}\hat{\boldsymbol{e}}\right)\right]\cdot\boldsymbol{\nabla}A\right\}\psi-k_BT\left[\frac{1}{\zeta_{\parallel}}\hat{\boldsymbol{e}}\hat{\boldsymbol{e}}+\frac{1}{\zeta_{\perp}}\left(\boldsymbol{I}-\hat{\boldsymbol{e}}\hat{\boldsymbol{e}}\right)\right]\cdot\boldsymbol{\nabla}\psi. \tag{2.28}$$

In the absence of an external velocity $\boldsymbol{v}_{ext}(\boldsymbol{r})=\boldsymbol{0}$, one can show the steady-state solution to the Smoluchowski equation (2.26) and the $\phi$-dynamics (2.17*a*) is the Boltzmann distribution:

$$\psi(\boldsymbol{r},\hat{\boldsymbol{e}},t\to\infty)\propto e^{-\frac{A[\phi(\boldsymbol{r}),\hat{\boldsymbol{e}}]}{k_BT}}\quad\text{and}\quad\frac{\delta A}{\delta\phi}=0, \tag{2.29}$$

where $A$ is the single-molecule free energy from (2.8):

$$A[\phi(\boldsymbol{r}),\hat{\boldsymbol{e}}]=F_{fluid}[\phi]+\chi\ell\hat{\boldsymbol{e}}\cdot\boldsymbol{\nabla}\phi(\boldsymbol{r}). \tag{2.30}$$

Thus, our hybrid discrete-particle–continuum-fluid model satisfies the detailed balance condition in the steady state, i.e. equilibrium.

To derive the local concentration of surfactant particles $c(\boldsymbol{r},t)$ and the local average orientation of the surfactant particles $\boldsymbol{p}(\boldsymbol{r},t)$, we expand the distribution function $\psi$ as in Appendix B. Inserting this into (2.26) and using the expression of the free energy in (2.30),



https://doi.org/10.1017/jfm.2026.11248 Published online by Cambridge University Press

we can write

$$\frac{\partial c(\boldsymbol{r},t)}{\partial t} = -\boldsymbol{\nabla}\cdot\left\{\boldsymbol{v}_{ext}(\boldsymbol{r})c(\boldsymbol{r},t) - \frac{\chi\ell c(\boldsymbol{r},t)}{d+2}\left[\left(\frac{1}{\zeta_\parallel}-\frac{1}{\zeta_\perp}\right)\boldsymbol{p}(\boldsymbol{r},t)\nabla^2\phi(\boldsymbol{r},t) + \left(\frac{2}{\zeta_\parallel}+\frac{d}{\zeta_\perp}\right)(\boldsymbol{p}(\boldsymbol{r},t)\cdot\boldsymbol{\nabla})\boldsymbol{\nabla}\phi(\boldsymbol{r},t)\right] - \frac{k_BT}{d}\mathrm{Tr}\left(\boldsymbol{\zeta}^{-1}\right)\boldsymbol{\nabla}c(\boldsymbol{r},t)\right\} \tag{2.31}$$

and

$$\begin{aligned}\frac{\partial(c(\boldsymbol{r},t)\boldsymbol{p}(\boldsymbol{r},t))}{\partial t} = &-\boldsymbol{\nabla}\cdot\left\{\boldsymbol{v}_{ext}(c\boldsymbol{p}) - \chi\ell\left(\frac{1}{\zeta_\parallel}-\frac{1}{\zeta_\perp}\right)\frac{c}{d(d+2)}\left(\boldsymbol{I}\nabla^2\phi+2\boldsymbol{\nabla}\boldsymbol{\nabla}\phi\right)\right.\\ &-\frac{\chi\ell}{\zeta_\perp}\frac{c(\boldsymbol{r},t)}{d}\boldsymbol{I}\nabla^2\phi - \frac{k_BT}{d+2}\left(\frac{1}{\zeta_\parallel}-\frac{1}{\zeta_\perp}\right)\left[\boldsymbol{\nabla}(c\boldsymbol{p})+\left(\boldsymbol{\nabla}(c\boldsymbol{p})\right)^T+\boldsymbol{I}\boldsymbol{\nabla}\cdot(c\boldsymbol{p})\right]\\ &\left.-\frac{k_BT}{\zeta_\perp}\left(\boldsymbol{\nabla}(c\boldsymbol{p})\right)^T\right\} - \frac{k_BT(d-1)}{\gamma_r}c\boldsymbol{p} - \frac{\chi\ell}{\gamma_r}\frac{d-1}{d}c\boldsymbol{\nabla}\phi + B\frac{d}{d+2}c\,\boldsymbol{D}_{ext}\cdot\boldsymbol{p}\\ &-c\,\boldsymbol{\Omega}_{ext}\cdot\boldsymbol{p}\end{aligned} \tag{2.32}$$

If one considers a hydrodynamic length scale $\xi$, then it is possible to determine the relative contributions of rotational and translational diffusion on this length scale. For rod-like particles,

$$\frac{\xi^2\zeta_\parallel}{\gamma_r} \sim \left(\frac{\xi}{\ell}\right)^2. \tag{2.33}$$

Therefore, when considering a length scale $\xi \gg \ell$, rotational diffusion is much faster than translational diffusion. On this length scale and in dimension $d$, the polarisation dynamics simplifies to

$$\frac{\partial\boldsymbol{p}(\boldsymbol{r},t)}{\partial t} + \boldsymbol{v}_{ext}(\boldsymbol{r})\cdot\boldsymbol{\nabla}\boldsymbol{p}(\boldsymbol{r},t) = -\frac{d-1}{d\gamma_r c(\boldsymbol{r},t)}\frac{\delta F}{\delta\boldsymbol{p}} + \left[B\frac{d}{d+2}\boldsymbol{D}_{ext}(\boldsymbol{r}) - \boldsymbol{\Omega}_{ext}(\boldsymbol{r})\right]\cdot\boldsymbol{p}(\boldsymbol{r},t) \tag{2.34}$$

and the concentration dynamics (taking $\zeta_\perp \approx \zeta_\parallel = \gamma_t$) are

$$\frac{\partial c(\boldsymbol{r},t)}{\partial t} = -\boldsymbol{\nabla}\cdot\left[\boldsymbol{v}_{ext}(\boldsymbol{r})c(\boldsymbol{r},t) - \frac{1}{\gamma_t}c(\boldsymbol{r},t)\boldsymbol{\nabla}\left(\frac{\delta F}{\delta c}\right)\right] \tag{2.35}$$

with the identification of a coarse-grained mesoscopic Helmholtz free energy:

$$F[\phi,c,\boldsymbol{p}] = \int d^dr\left[\frac{\alpha}{2}\phi^2+\frac{\beta}{4}\phi^4+\frac{\kappa}{2}|\boldsymbol{\nabla}\phi|^2 + k_BTc\ln(a^dc) + \chi\ell c\boldsymbol{p}\cdot\boldsymbol{\nabla}\phi + \frac{d}{2}k_BTc|\boldsymbol{p}|^2\right] \tag{2.36}$$

where $a$ is the typical microscopic length scale, introduced to make the term inside the logarithm dimensionless (the addition term $c\ln(a^d)$ drops out in the dynamics). The first two terms, $\alpha\phi^2/2$ and $\beta\phi^4/4$, are standard Cahn–Hilliard terms derived from thermodynamic theory (Lee *et al.* 2014), where $\alpha$ and $\beta$ are constants that characterise the behaviour of the two phases. These terms form a double well potential representing the water and oil phases. Setting $\alpha<0$ and $\beta>0$ ensures that the two fluids remain distinct and do not mix. The third term, $\kappa|\boldsymbol{\nabla}\phi|^2/2$, is a semi-local term responsible for creating the diffuse water–oil interface, with $\kappa$ controlling the width of the interface. In particular, the width of the diffuse interface is given by $\xi_I = \sqrt{-2\kappa/\alpha}$ (Cates & Tjhung 2018). The logarithmic term $k_BTc\ln(a^dc)$ captures the translational diffusion



https://doi.org/10.1017/jfm.2026.11248 Published online by Cambridge University Press

of the surfactant molecules. Similarly, the term $dk_BTc|\boldsymbol{p}|^2/2$ accounts for the rotational diffusion. The term $\chi\ell c\boldsymbol{p}\cdot\nabla\phi$ couples the surfactants to the fluid, causing them to be attracted and align perpendicular to the interface. In the absence of surfactant, $c=0$ or $\chi=0$, the bare surface tension of the water–oil interface is given by $\sigma_I=\sqrt{-8\kappa\alpha^3/(9\beta^2)}$. Equation (2.36) can alternatively be derived from direct calculation of the Shannon entropy and energy contributions to the Helmholtz free energy, as shown in Appendix A.

We emphasise that the coarse-grained mesoscopic free energy $F$ is distinct from the hybrid single-molecule–continuum-fluid free energy $A$ in (2.8), which depends explicitly on the discrete particle position. In the absence of external flow, $\boldsymbol{v}_{ext}=0$, one can show that the steady-state solution to the $\boldsymbol{p}$- and $c$-dynamics in (2.34) and (2.35), respectively, is given by the minimum of the coarse-grained mesoscopic free energy:

$$\frac{\delta F}{\delta c}=0 \quad \text{and} \quad \frac{\delta F}{\delta \boldsymbol{p}}=\boldsymbol{0}. \tag{2.37}$$

This shows that the detailed balance property is preserved under coarse-graining: at the single-particle level, the equilibrium steady state is characterised by a Boltzmann distribution (see (2.29)), while at the coarse-grained level, it corresponds to the minimum of the mesoscopic free energy $F$.

### 2.3. *Coupling surfactant particle dynamics back to the fluid flow.*

The results of the previous subsection neglect hydrodynamic effects due to the presence of the surfactants, as can be seen in the definition of $\boldsymbol{v}_{ext}(\boldsymbol{r})$ in (2.19). To derive hydrodynamic flows from the surfactants, we again use the Rayleigh dissipation formalism. However, we now start with the coarse-grained free energy of (2.36) in our definition of the Rayleighian, so that (cf. (2.9))

$$\mathcal{R}_{cg}[\partial_t\phi,\,\boldsymbol{v},\,\boldsymbol{v}_1,\,\partial_t c,\,\partial_t\boldsymbol{p}]=\Phi_1[\boldsymbol{v}]+\Phi_2[\boldsymbol{v}_1,\,\boldsymbol{v}_2]+\dot{F}, \tag{2.38}$$

where

$$\dot{F}=\int d^3r\left(\frac{\delta F}{\delta\phi}\partial_t\phi+\frac{\delta F}{\delta c}\partial_t c+\frac{\delta F}{\delta\boldsymbol{p}}\partial_t\boldsymbol{p}\right). \tag{2.39}$$

Here, $\partial_t\phi$, $\partial_t c$ and $\partial_t\boldsymbol{p}$ are defined in (2.17*a*), (2.35) and (2.34). Within these equations, we replace the external field $\boldsymbol{v}_{ext}\to\boldsymbol{v}$, where $\boldsymbol{v}(\boldsymbol{r},t)$ is now the total fluid velocity to be determined self-consistently, so

$$\frac{\partial\phi(\boldsymbol{r},t)}{\partial t}+\nabla\cdot[\phi(\boldsymbol{r},t)\boldsymbol{v}(\boldsymbol{r},t)]=M\nabla^2\frac{\delta F}{\delta\phi}, \tag{2.40a}$$

$$\frac{\partial c(\boldsymbol{r},t)}{\partial t}+\nabla\cdot[c(\boldsymbol{r},t)\boldsymbol{v}(\boldsymbol{r},t)]=\nabla\cdot\left[\frac{1}{\gamma_t}c(\boldsymbol{r},t)\nabla\left(\frac{\delta F}{\delta c}\right)\right], \tag{2.40b}$$

$$\frac{\partial\boldsymbol{p}(\boldsymbol{r},t)}{\partial t}+\boldsymbol{v}(\boldsymbol{r},t)\cdot\nabla\boldsymbol{p}(\boldsymbol{r},t)=-\frac{d-1}{d\gamma_r c(\boldsymbol{r},t)}\frac{\delta F}{\delta\boldsymbol{p}}+\left[\frac{Bd}{d+2}\boldsymbol{D}(\boldsymbol{r},t)-\boldsymbol{\Omega}(\boldsymbol{r},t)\right]\cdot\boldsymbol{p}(\boldsymbol{r},t), \tag{2.40c}$$

where $F$ is given in (2.36). Inserting these equations into the free energy dissipation and taking functional derivatives with respect to $\boldsymbol{v}$ and $\boldsymbol{v}_1$ (with $\boldsymbol{v}=(1+\phi)\boldsymbol{v}_1/2+(1-\phi)\boldsymbol{v}_2/2$), we find the Stokes equation



https://doi.org/10.1017/jfm.2026.11248 Published online by Cambridge University Press

$$0 = \eta\nabla^2\boldsymbol{v} - \nabla P - (1+\phi)\nabla\frac{\delta F}{\delta\phi} - c\nabla\frac{\delta F}{\delta c} - \boldsymbol{p}\cdot\left(\nabla\frac{\delta F}{\delta \boldsymbol{p}}\right)^T + \frac{Bd}{2(d+2)}\nabla\cdot\left(\boldsymbol{p}\frac{\delta F}{\delta \boldsymbol{p}} + \frac{\delta F}{\delta \boldsymbol{p}}\boldsymbol{p}\right) - \frac{1}{2}\nabla\cdot\left(\boldsymbol{p}\frac{\delta F}{\delta \boldsymbol{p}} - \frac{\delta F}{\delta \boldsymbol{p}}\boldsymbol{p}\right) \tag{2.41}$$

where $P$ is the pressure enforcing incompressibility $\nabla\cdot\boldsymbol{v} = 0$. Note that the $-\nabla\delta F/\delta\phi$ term in (2.41) can be absorbed into the pressure term $-\nabla P$. Equations (2.40) and (2.41) completely describe the dynamics of the surfactant in a binary fluid system for the case of non-interacting surfactant molecules (they are only interacting through the fluid velocity). The mathematical structure of the stress-like tensor in the Stokes equation (2.41) is consistent with the Cauchy stress previously obtained for polar liquid crystals (Cates & Tjhung 2018; Markovich, Tjhung & Cates (2019).

In the absence of external driving, minimising the Rayleighian dissipation functional yields the equilibrium equations of motion for the system. When a flow field is imposed, e.g. a shear flow, the Rayleighian simply acquires an additional contribution associated with the externally driven fluid flow. Minimising this modified functional produces the full equations governing both the transient dynamics and the resulting non-equilibrium steady state. Thus, the Rayleighian formalism provides a unified description of equilibrium and driven non-equilibrium behaviour, without the need for separate modelling assumptions.

## 3. Results and discussion

To demonstrate the validity and reliability of our model, we present three case studies. The first examines a planar interface under the assumption of weak coupling, where we show that the system equations can be solved analytically via perturbation theory to any desired order. Numerical results are also provided, showing excellent agreement with our analytical solutions. The second case study extends this system by using the perturbative solutions to calculate the surface tension of a surfactant-loaded interface, where the presence of surfactants leads to a decrease in surface tension. Finally, we demonstrate how the inclusion of surfactants may suppress the coalescence of oil droplets.

### 3.1. *Non-dimensionalisation and numerical method of solution*

All of the following simulation results are presented in dimensionless units. Without loss of generality, we set $\alpha = -\beta$ in the free energy expression (2.36), so that the bulk free energy favours phase separation into $\phi = \pm 1$. We choose the interfacial width of the pure binary fluid, $\xi_I = \sqrt{2\kappa/\beta}$ as the unit of length, $\tau$ as the unit of time and $k_BT$ as the unit of energy. We also introduce a small (dimensionless) parameter $\varepsilon = \chi\ell/(\xi_I k_B T)$ to represent the weak coupling between the fluid and surfactants. Physically, $\varepsilon$ characterises the interaction strength between the surfactant molecules and the binary fluid interface (relative to $k_BT$). For simplicity, we retain the same notation for the non-dimensionalised constants and variables as in the dimensional forms. More details can be found in Appendix C. The dimensionless Helmholtz free energy is then given by

$$F[\phi, c, \boldsymbol{p}] = \int\left\{-\frac{\beta}{2}\phi^2 + \frac{\beta}{4}\phi^4 + \frac{\beta}{4}|\nabla\phi|^2 + c\ln(c) + \frac{d}{2}c|\boldsymbol{p}|^2 + \varepsilon c\boldsymbol{p}\cdot\nabla\phi\right\}d^dr, \tag{3.1}$$

and the resulting system of coupled partial differential equations governing the dynamics of the binary fluid volume fraction, surfactant concentration, average orientation field and fluid velocity can be expressed as



https://doi.org/10.1017/jfm.2026.11248 Published online by Cambridge University Press

$$\frac{\partial \phi}{\partial t} + (\boldsymbol{v}\cdot\boldsymbol{\nabla})\phi = M\nabla^2\left(\frac{\delta F}{\delta \phi}\right) = M\nabla^2\left[-\beta\phi + \beta\phi^3 - \frac{\beta}{2}\nabla^2\phi - \varepsilon\boldsymbol{\nabla}\cdot(c\boldsymbol{p})\right], \tag{3.2a}$$

$$\frac{\partial c}{\partial t} + (\boldsymbol{v}\cdot\boldsymbol{\nabla})c = \boldsymbol{\nabla}\cdot\left[\frac{c}{\gamma_t}\boldsymbol{\nabla}\left(\frac{\delta F}{\delta c}\right)\right] = \frac{1}{\gamma_t}\nabla^2 c + \frac{1}{\gamma_t}\boldsymbol{\nabla}\cdot\left[c\boldsymbol{\nabla}\left(\frac{d}{2}|\boldsymbol{p}|^2 + \varepsilon\boldsymbol{p}\cdot\boldsymbol{\nabla}\phi\right)\right], \tag{3.2b}$$

$$\frac{\partial \boldsymbol{p}}{\partial t} + (\boldsymbol{v}\cdot\boldsymbol{\nabla})\boldsymbol{p} + \boldsymbol{\Omega}\cdot\boldsymbol{p} - \frac{B\mathrm{d}}{d+2}\boldsymbol{D}\cdot\boldsymbol{p} = -\frac{d-1}{d\gamma_r c}\left(\frac{\delta F}{\delta \boldsymbol{p}}\right) = -\frac{d-1}{d\gamma_r}(\mathrm{d}\boldsymbol{p} + \varepsilon\boldsymbol{\nabla}\phi), \tag{3.2c}$$

$$0 = -\boldsymbol{\nabla}P + \eta\nabla^2\boldsymbol{v} + \boldsymbol{f} + \boldsymbol{\nabla}\cdot\boldsymbol{\sigma}, \tag{3.2d}$$

$$0 = \boldsymbol{\nabla}\cdot\boldsymbol{v}, \tag{3.2e}$$

where we have defined the body force

$$\boldsymbol{f} \equiv -\phi\boldsymbol{\nabla}\frac{\delta F}{\delta \phi} - c\boldsymbol{\nabla}\frac{\delta F}{\delta c} - \boldsymbol{p}\cdot\left(\boldsymbol{\nabla}\frac{\delta F}{\delta \boldsymbol{p}}\right)^T \tag{3.3}$$

and the stress-like tensor

$$\boldsymbol{\sigma} \equiv \frac{Bd}{2(d+2)}\left(\boldsymbol{p}\frac{\delta F}{\delta \boldsymbol{p}} + \frac{\delta F}{\delta \boldsymbol{p}}\boldsymbol{p}\right) - \frac{1}{2}\left(\boldsymbol{p}\frac{\delta F}{\delta \boldsymbol{p}} - \frac{\delta F}{\delta \boldsymbol{p}}\boldsymbol{p}\right). \tag{3.4}$$

In the dimensionless unit, the bare surface tension is then given by $\sigma_I = 2\beta/3$. For the remainder of this paper, we consider the two-dimensional case ($d = 2$) only.

In the following, we briefly outline the general numerical scheme employed in our study, based on the dimensionless (3.2). We consider a two-dimensional domain of size $L_x$ in the $x$-direction and $L_y$ in the $y$-direction. We employ a simple finite difference method with Euler time-stepping to simulate the variables $\phi(\boldsymbol{r}, t)$, $c(\boldsymbol{r}, t)$ and $\boldsymbol{p}(\boldsymbol{r}, t)$. This is implemented using the Python library NumPy (Harris *et al.* 2020). Central differences are used for both first- and second-order derivatives. We assume periodic boundary conditions at $y = 0$ and $y = L_y$. Boundary conditions at $x = 0$ and $x = L_x$ can either be no-flux or periodic. No-flux conditions are derived to conserve $\phi(\boldsymbol{r}, t)$ and $c(\boldsymbol{r}, t)$, resulting in either Neumann or reflective boundary conditions, as detailed in Appendix D. Unless otherwise specified, the values for all parameters used in the simulations are provided in Appendix C.

At each time step, the fluid velocity $\boldsymbol{v}$ is calculated using a pseudospectral method as outlined by Hardy *et al.* (2024). By transforming the Stokes equation (3.2*d*) into Fourier space (where Fourier-space variables are denoted with a tilde), we obtain the expression used to calculate the velocity at each time step:

$$\widetilde{\boldsymbol{v}}_{\boldsymbol{k}} = \frac{1}{\eta k^2}\left[\widetilde{\boldsymbol{f}}_{\boldsymbol{k}} - \left(\widetilde{\boldsymbol{f}}_{\boldsymbol{k}}\cdot\hat{\boldsymbol{k}}\right)\hat{\boldsymbol{k}}\right], \tag{3.5}$$

where $\boldsymbol{k}$ is the wavevector, $k = |\boldsymbol{k}|$ is the corresponding wavenumber and $\hat{\boldsymbol{k}} = \boldsymbol{k}/k$ is the unit wavevector. The forcing term $\widetilde{\boldsymbol{f}}_{\boldsymbol{k}}$ encompasses all terms from $\boldsymbol{f}$ and $\boldsymbol{\nabla}\cdot\boldsymbol{\sigma}$. The Fourier-space pressure is

$$\widetilde{P}_{\boldsymbol{k}} = -\frac{i}{k}\widetilde{\boldsymbol{f}}_{\boldsymbol{k}}\cdot\hat{\boldsymbol{k}}. \tag{3.6}$$

As with $\phi$, $c$ and $\boldsymbol{p}$, we impose periodic boundary conditions on $\boldsymbol{v}$ at $y = 0$ and $y = L_y$. Along the $x$-direction, the fluid velocity $\boldsymbol{v}$ can satisfy either no-slip or periodic boundary conditions. In the case of no-slip boundary conditions at $x = 0$ and $x = L_x$, combined with



https://doi.org/10.1017/jfm.2026.11248 Published online by Cambridge University Press

periodic boundary conditions at $y = 0$ and $y = L_y$, it is convenient to use a sine transform in $x$ and a standard Fourier transform in $y$, i.e.

$$\boldsymbol{v}(\boldsymbol{r}) = \sqrt{\frac{2}{L_x L_y}} \sum_{n,m} \widetilde{\boldsymbol{v}}_{\boldsymbol{k}} \sin\left(\frac{n\pi x}{L_x}\right) e^{i\frac{2\pi m y}{L_y}}, \tag{3.7}$$

where $n = 1, 2, 3, \ldots$ and $m \in \mathbb{Z}$. The corresponding discrete wavevector $\boldsymbol{k} = (k_x, k_y)^T$ are given by $k_x = \pi n / L_x$ and $k_y = 2\pi m / L_y$, see https://github.com/AlexHardy0/Surfactants for detailed implementation.

We validated our model by simulating a pure binary fluid and obtaining the classical solution for a clean binary fluid (Cates & Tjhung 2018). The pseudospectral scheme used for velocity was also validated through the Poiseuille flow example, where it perfectly matched the analytical solutions.

### 3.2. *Planar interface*

Our first case study involves a flat, vertical water–oil interface at $x = 0$, as shown in figure 3(*b*). Over time, surfactants adsorb onto the interface, resulting in a peak in concentration $c(\boldsymbol{r}, t)$, although some surfactant concentration remains in the bulk phases. Additionally, the surfactant molecules align perpendicular to the interface, with the 'head' in the water phase and the 'tail' in the oil phase, as indicated by the non-zero $x$-component of $\boldsymbol{p}(\boldsymbol{r}, t)$. When $|\boldsymbol{p}| > 0$, the molecules are aligned, as opposed to being randomly arranged when $\boldsymbol{p} \approx \boldsymbol{0}$. At equilibrium, the fluid velocity falls to zero and the system reaches a static configuration. Assuming $\varepsilon = \chi \ell / (\xi_I k_B T) \ll 1$, we can solve the steady-state solution perturbatively.

We now solve the system of nonlinear ordinary differential equation (3.2) (with $d = 2$) using a regular perturbation approach. Due to translational symmetry in the $y$-direction, the solutions depend only on the $x$-direction. At steady-state equilibrium, the system equations then simplify to

$$\beta\left(\phi - \phi^3 + \frac{1}{2}\phi''\right) + \varepsilon\,(c p_x)' = 0, \tag{3.8a}$$

$$c' + c(p_x^2)' + \varepsilon c (p_x \phi')' = 0, \tag{3.8b}$$

$$2p_x + \varepsilon \phi' = 0, \tag{3.8c}$$

where $p_x$ is the $x$-component of the field $\boldsymbol{p}(\boldsymbol{r}, t)$. Here, primes indicate differentiation with respect to $x$. It follows from (3.8*c*) that

$$p_x = -\frac{1}{2}\varepsilon \phi'. \tag{3.9}$$

Thus, we only need to find the solution for the fields $\phi$ and $c$. Substituting (3.9) into (3.8*a*) and (3.8*b*), we obtain

$$\beta\left(2\phi - 2\phi^3 + \phi''\right) - \varepsilon^2\,(c\phi')' = 0, \tag{3.10a}$$

$$2c' + \varepsilon^2 c \phi' \phi'' - \varepsilon^2 c (\phi'^2)' = 0. \tag{3.10b}$$

Equations (3.10) are highly nonlinear, making an analytical solution challenging. To address this, we seek an approximate solution using the perturbation method, expressing the solution as



https://doi.org/10.1017/jfm.2026.11248 Published online by Cambridge University Press

$$\phi(x) = \phi_0(x) + \phi_2(x)\,\varepsilon^2 + \phi_4(x)\,\varepsilon^4 + \mathcal{O}(\varepsilon^6), \tag{3.11a}$$

$$c(x) = c_0(x) + c_2(x)\,\varepsilon^2 + c_4(x)\,\varepsilon^4 + \mathcal{O}(\varepsilon^6). \tag{3.11b}$$

Due to parity considerations, we expect the odd powers in the series expansions of $\phi$ and $c$ to vanish. Inserting the perturbation expansion into (3.10) yields the zeroth-order problem as

$$\phi_0'' + 2\phi_0 - 2\phi_0^3 = 0, \tag{3.12a}$$

$$c_0' = 0, \tag{3.12b}$$

the solution of which is given by

$$\phi_0(x) = \tanh x, \tag{3.13a}$$

$$c_0(x) = C_0 = \text{const.}, \tag{3.13b}$$

where tanh represents the hyperbolic tangent function and $C_0$ is some constant. To simplify the equations, we introduce the abbreviation $\lambda = C_0/\beta$ as well as the function $S(x) = \operatorname{sech}^2 x$. The order $\varepsilon^2$ equations are obtained as

$$\beta\phi_2'' + 2\beta\big(1 - 3\phi_0^2\big)\phi_2 - C_0\phi_0'' = 0, \tag{3.14a}$$

$$2c_2' - C_0\phi_0'\phi_0'' = 0. \tag{3.14b}$$

The solution to this is given by

$$\phi_2(x) = \frac{1}{2}\,\lambda x S(x), \tag{3.15a}$$

$$c_2(x) = \frac{1}{4}\,C_0 S(x)^2. \tag{3.15b}$$

The equations at order $\varepsilon^4$ are given by

$$\beta\phi_4'' + 2\beta(1 - 3\phi_0^2)\phi_4 = c_2\phi_0'' + C_0\phi_2'' + c_2'\phi_0' + 6\beta\phi_0\phi_2^2, \tag{3.16a}$$

$$2c_4' = C_0\phi_0'\phi_2'' + \big(C_0\phi_2' + c_2\phi_0'\big)\,\phi_0''. \tag{3.16b}$$

The solution to this is given by

$$\phi_4(x) = \frac{1}{16}\,\lambda S(x)\big(6\lambda x + \big(2 - 4\lambda x^2 + S(x)\big)\tanh x\big), \tag{3.17a}$$

$$c_4(x) = \frac{1}{32}\,C_0 S(x)^2\big(8\lambda(1 - 2x\tanh x) + S(x)^2\big). \tag{3.17b}$$

In theory, we could extend beyond the current order and determine higher-order terms in the perturbation series. However, due to technical limitations and the complexity of the resulting expressions, we stop at the current order. We expect the series to provide an accurate approximation of the solution, provided that $\varepsilon \ll 1$.

From (3.9), it follows that the polarisation can be expressed as an odd power series in $\varepsilon$, given by

$$p_x(x) = p_{x1}(x)\varepsilon + p_{x3}(x)\varepsilon^3 + p_{x5}(x)\varepsilon^5 + \mathcal{O}(\varepsilon^7). \tag{3.18}$$

We find after calculation that

$$p_{x1}(x) = -\frac{1}{2}\,S(x), \tag{3.19a}$$

$$p_{x3}(x) = \frac{1}{4}\,\lambda S(x)\,(2x\tanh x - 1)\,, \tag{3.19b}$$



https://doi.org/10.1017/jfm.2026.11248 Published online by Cambridge University Press

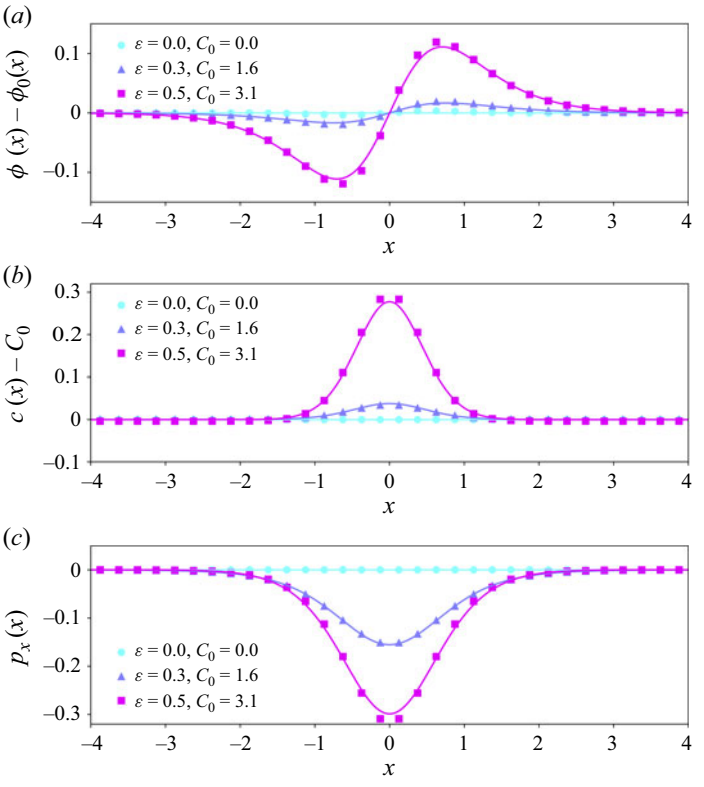



Figure 2. (*a*) A graph showing the analytical (line) and numerical (symbols) solutions for the fluid field $\phi(x)$ with the leading order $\phi_0(x) = \tanh x$ removed, at equilibrium for a variety of $\varepsilon$ and $C_0$ values. (*b*) A graph showing the analytical (line) and numerical (symbols) solutions for concentration $c(x)$ with the leading order $c_0(x) = C_0$ removed, at equilibrium for a range of $\varepsilon$ and $C_0$ values. (*c*) A graph showing the analytical (line) and numerical (symbols) solutions for the polarisation field $p_x(x, t)$, at equilibrium for a range of $\varepsilon$ and $C_0$ values. Parameters used: $\beta = 2.0$, $B = 0.5$, $M = 3$, $\gamma_t = \gamma_r = 0.01$.

$$p_{x5}(x) = \frac{1}{32}\,\lambda S(x)\big(4 - 6\lambda - 8\lambda x^2 + 20\lambda x \tanh x + (12\lambda x^2 - 2)S(x) - 5S(x)^2\big). \tag{3.19c}$$

For comparison, we also simulate the same scenario using the numerical scheme described in § 3.1. We use a two-dimensional rectangular computational domain sized $L_x = 64$ and $L_y = 4$ with a spatial resolution of $\Delta x = \Delta y = 0.25$ and temporal resolution of $\Delta t = 0.0001$. We use a uniform initial condition for $c(\boldsymbol{r}, t)$, with initial concentration value $c(\boldsymbol{r}, t = 0) = C_0$. Physically, $C_0$ represents the average surfactant concentration, which is conserved throughout. Volume fraction field $\phi(\boldsymbol{r}, t)$ is initialised as two halves, with $\phi(x < 0) = -1.0$ (water) and $\phi(x > 0) = 1.0$ (oil). Each phase has a magnitude of 1 as that is the solution of the double well potential in the free energy density. All other fields are initialised as zero everywhere. We have periodic boundary conditions at $y = 0$ and $y = L_y$, and no-slip/no-flux boundary conditions at $x = -L_x/2$ and $x = L_x/2$. This is to ensure that only one water–oil interface is created. We choose to vary two parameters, $\varepsilon$ and the average surfactant concentration $C_0$. Three simulations were run in total, with parameters: $\varepsilon = 0.0$ and $C_0 = 0$ (clean system), one with $\varepsilon = 0.3$ and $C_0 = 1.6$, and another with $\varepsilon = 0.5$ and $C_0 = 3.1$.

Figure 2 show the steady-state profiles $\phi(x, t \to \infty)$, $c(x, t \to \infty)$ and $p_x(x, t \to \infty)$, demonstrating excellent agreement with the perturbation theory. The deviations in $\phi(\boldsymbol{r}, t)$



https://doi.org/10.1017/jfm.2026.11248 Published online by Cambridge University Press

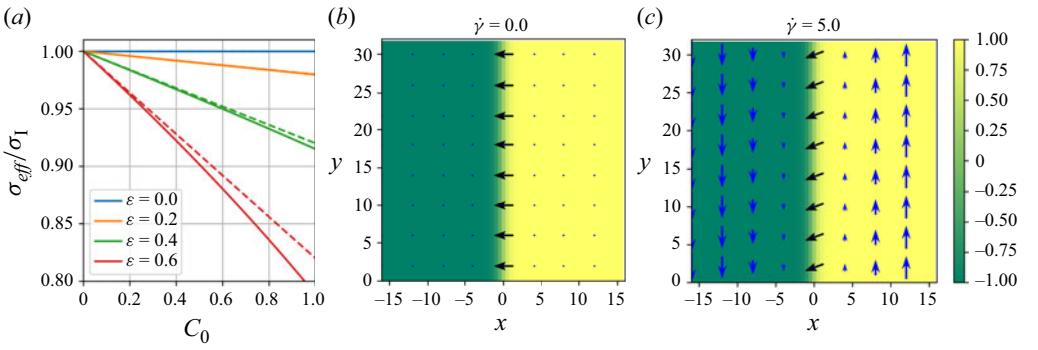



Figure 3. (*a*) Effective surface tension divided by the bare surface tension $\sigma_{eff}/\sigma$I as a function of bulk surfactant concentration $C_0$ for different values of coupling strength $\varepsilon$ and fixed $\beta = 1$. Dashed lines indicate the leading-order prediction from the Gibbs isotherm. (*b*) Equilibrium configuration of a planar interface located at $x = 0$. Black arrows show the polarisation field $\boldsymbol{p}$ which aligns perpendicular to the interface. (*c*) Under strong shear flow, the polarisation $\boldsymbol{p}$ field becomes tilted and is no longer perpendicular to the interface. Blue arrows indicate the fluid velocity $\boldsymbol{v}$. Parameters used: $\beta = 1.0$, $B = 1.0$, $M = 1.0$, $\gamma_t = \gamma_r = 0.1$, $\eta = 1.0$ and $\varepsilon = 0.5$.

remain small relative to the bulk values ($\pm 1$), indicating that the fluid is only weakly perturbed, consistent with earlier studies, which also assume weak coupling between the fluid density and surfactant concentrations (van der Sman & van der Graaf 2006; Liu & Zhang 2010), although these studies did not incorporate an explicit polarisation field $\boldsymbol{p}(\boldsymbol{r}, t)$. As expected, the magnitude of deviations increases with both the coupling strength $\varepsilon$ and the mean surfactant concentration $C_0$. The concentration profile $c(\boldsymbol{r}, t \to \infty)$ exhibits a peak localised around the interface, with enhancements of the order of 0.2, comparable to values reported in prior numerical studies (van der Sman & van der Graaf 2006; Liu & Zhang 2010; Zong *et al.* 2020), again in the absence of a polarisation field.

As $\varepsilon$ increases, more surfactant molecules are adsorbed at the interface due to the stronger attraction, leading to a higher peak in the surfactant concentration. The absorbed molecules exhibit alignment, as indicated by the peak in $p_x(x, t \to \infty)$ near the interface. Since the leading-order contribution to $p_x(x, t \to \infty)$ is zero, this peak arises entirely from perturbative corrections. At equilibrium, molecular orientation at the interface exhibits minimal noise, with the $y$-component of $\boldsymbol{p}(\boldsymbol{r}, t \to \infty)$ remaining negligible. We observe little dependence of the alignment strength on $C_0$, indicating that increasing the number of adsorbed surfactant molecules does not significantly affect their collective orientation. Instead, alignment is more strongly governed by the coupling strength $\varepsilon$, which determines the effective attraction to the interface. Overall, the simulations show excellent agreement with the perturbative theory and are consistent with established understanding of surfactant behaviour at fluid interfaces at microscopic level.

### 3.3. *Adsorption isotherm and effective surface tension*

Let us consider a flat interface at $x = 0$ with $\phi(x < 0) < 0$ (water phase) and $\phi(x > 0) > 0$ (oil phase), as shown in figure 3(*b*). The concentration profile $c(x)$ across this interface has been solved perturbatively in (3.11*b*) and plotted in figure 2(*b*). In experiments, the volumetric concentration of surfactant at an oil–water interface is typically $10^2$–$10^4$ times larger than the bulk concentration (Faria & Vishnyakov 2022), far exceeding the interfacial concentrations reached in our simulations. This occurs because real fluid interfaces are extremely sharp: the interfacial width is of the order of a molecular length scale. By contrast, in simulations, we employ a diffuse-interface (phase-field) model, in which the interface is spread over a finite width $\xi_I$. For numerical stability and resolution, $\xi_I$ is usually



https://doi.org/10.1017/jfm.2026.11248 Published online by Cambridge University Press

taken to be several orders of magnitude larger than its physical, molecular-scale value (Jaensson, Hulsen & Anderson 2017). Instead, we quantify adsorption by measuring the amount of surfactant adsorbed per unit interfacial area,

$$\Gamma = \int_{-\infty}^{\infty} [c(x) - C_0]\,\mathrm{d}x. \tag{3.20}$$

Substituting the perturbative solution for $c(x)$ in (3.11*b*) to (3.20), we obtain

$$\Gamma = \frac{1}{3}\epsilon^2 C_0 + \mathcal{O}(\epsilon^4). \tag{3.21}$$

Thus, the amount of adsorbed surfactant increases linearly with the bulk concentration $C_0$. This is consistent with the Henry's law adsorption isotherm in the dilute surfactant limit (van der Sman & van der Graaf 2006). A full quantitative comparison with adsorption–desorption kinetics would require extending the model to include finite-rate kinetic terms that explicitly describe the adsorption and desorption of molecules at the interface.

We can now compute the reduction in effective surface tension $\sigma_{eff}$ induced by the adsorption of surfactant molecules at the interface. To do so, we first define the grand potential functional to be

$$\Phi[\phi, c, \boldsymbol{p}] = F[\phi, c, \boldsymbol{p}] - \bar{\mu}_c \int c(\boldsymbol{r})\, d^d r \equiv \int w(\boldsymbol{r})\, d^d r, \tag{3.22}$$

where $w(\boldsymbol{r})$ denotes the grand potential density. The constant $\bar{\mu}_c$ is the chemical potential of an external surfactant reservoir, corresponding to the grand canonical ensemble. Mathematically, the grand potential $\Phi[\phi, c, \boldsymbol{p}]$ is a Legendre transform of the Helmholtz free energy $F[\phi, c, \boldsymbol{p}]$ with respect to $c$. In equilibrium, the condition $\delta F/\delta c = \bar{\mu}_c$ yields $\bar{\mu}_c = \log(C_0) + 1$. The effective surface tension $\sigma_{eff}$ is then defined to be the excess grand potential per unit area of the interface:

$$\sigma_{eff} = \int_{-\infty}^{\infty} [w(x) - w_{bulk}]\ \mathrm{d}x, \tag{3.23}$$

where $w_{bulk}$ is the value of the grand potential density evaluated in the bulk, i.e. in the limit $x \to \pm\infty$, or far from the interface. Using the perturbative solutions for $\phi(x)$, $c(x)$ and $p_x(x)$ from § 3.2, (3.23) can then be computed numerically, retaining terms up to order $\mathcal{O}(\varepsilon^6)$. The resulting effective surface tension $\sigma_{eff}$ as a function of the bulk surfactant concentration $C_0$ is shown in figure 3(*a*) (solid lines). As expected, $\sigma_{eff}$ approaches the bare interfacial value $\sigma_I = 2\beta/3$ of the clean binary fluid in the limit $C_0 \to \infty$. For comparison, we may also invoke the Gibbs adsorption isotherm, which in dimensionless form reads

$$\frac{\mathrm{d}\sigma_{eff}}{\mathrm{d}\ln C_0} = -\Gamma. \tag{3.24}$$

Substituting the expression for $\Gamma$ from (3.21) and integrating, we obtain the explicit leading-order result for the effective surface tension

$$\sigma_{eff} = \sigma_I - \frac{\varepsilon^2}{3} C_0 + \mathcal{O}(\varepsilon^4). \tag{3.25}$$

The corresponding prediction from the Gibbs isotherm is shown in figure 3(*a*) (dashed lines), where it agrees with our direct definition of $\sigma_{eff}$ in (3.23).

Finally, we note that the effective surface tension shown in figure 3(*a*) applies only under equilibrium conditions. At equilibrium, the fluid velocity vanishes $\boldsymbol{v} = \boldsymbol{0}$, and the fluid composition $\phi$, surfactant concentration $c$ and polarisation $\boldsymbol{p}$ relax to the configuration



https://doi.org/10.1017/jfm.2026.11248 Published online by Cambridge University Press

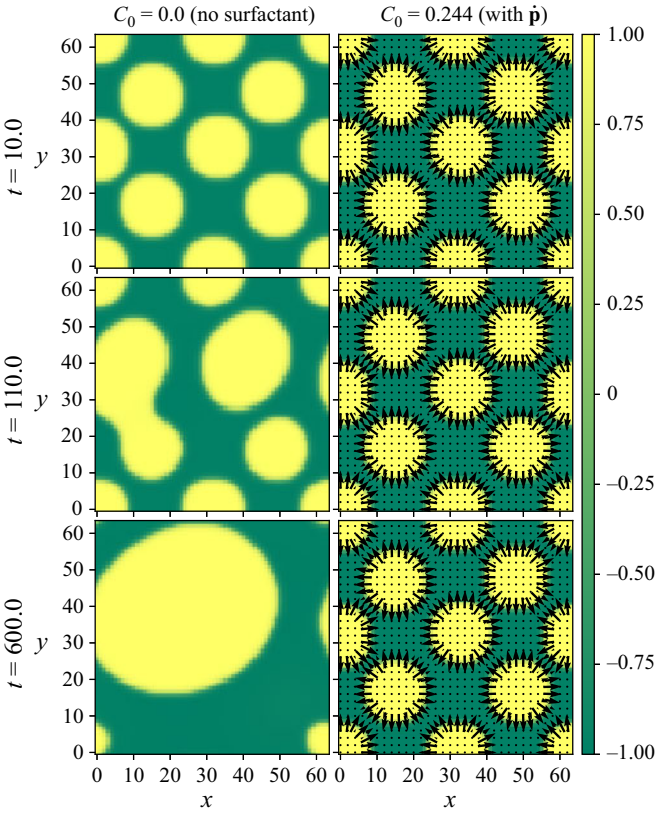



Figure 4. Plots of binary fluid volume fraction $\phi(\boldsymbol{r}, t)$ for bare emulsion ($a$) and surfactant-containing emulsion ($b$) at different time steps (rows) with values $t = 10$, 110 and 600 being the first, second and third rows, respectively. The black arrows on the right column indicate the polarisation or average orientation of the surfactant molecules, $\boldsymbol{p}(\boldsymbol{r}, t)$. The graphs show that the presence of the surfactants suppresses droplet coalescence and full phase separation. Parameters used: ($\varepsilon = 0$, $C_0 = 0$) ($a$) and ($\varepsilon = 1.5$, $C_0 = 0.244$) ($b$). Other parameters: $\beta = 2$, $B = 0.5$, $M = 3$ and $\gamma_t = \gamma_r = 0.01$.

which minimises the free energy in (3.1). In this state, the polarisation field $\boldsymbol{p}$ aligns strictly perpendicular to the interface, see figure 3($b$). In contrast, when the system is subjected to a strong shear flow, for example, $\boldsymbol{v} \simeq \dot{\gamma} x \hat{\boldsymbol{y}}$, the polarisation $\boldsymbol{p}$ is oriented by the flow and becomes tilted relative to the interface normal vector, see figure 3($c$). This shear-induced reorientation modifies the local interfacial stresses and, consequently, can change the effective surface tension.

### 3.4. *Emulsion study*

Our final case study examines an emulsion of oil droplets suspended in water, with the initial condition shown in the first row of figure 4. Simulations were performed on a $L_x \times L_y = 64 \times 64$ grid with spatial resolution $\Delta x = \Delta y = 0.5$ and time step $\Delta t = 0.001$. To compare the effects of surfactants, we conducted two simulations: one for a clean system with no surfactants ($\varepsilon = 0$, $C_0 = 0$) and one with surfactants present ($\varepsilon = 1.5$, $C_0 = 0.244$). Periodic boundary conditions were applied along all edges of the domain ($x = 0$, $x = L_x$, $y = 0$, $y = L_y$).

In the absence of surfactants, the droplets gradually coalesce into a single large drop. By contrast, when surfactants are present, coalescence is significantly suppressed, leading



https://doi.org/10.1017/jfm.2026.11248 Published online by Cambridge University Press

to a more stable emulsion – although the system will still slowly evolve towards full phase separation over longer time scales. This stabilisation arises from the polarisation field $\boldsymbol{p}(\boldsymbol{r}, t)$: the surfactant molecules orient outwards from each droplet, generating effective repulsive interactions that hinder droplet merging. As shown in figure 4, the clean system (figure 4*a*) exhibits progressive coalescence, whereas the system with surfactants (figure 4*b*) retains a dispersed droplet morphology over the duration of the simulation. Although not shown, we note that increasing the mean surfactant concentration $C_0$ further suppresses coalescence, much like increasing the interaction strength $\varepsilon$. Finally, as shown in figure 4(*b*), the surfactant orientation vectors $\boldsymbol{p}(\boldsymbol{r}, t)$ point outwards from each droplet. In this configuration, adjacent droplets effectively experience mutual repulsion due to opposing molecular orientations, thereby maintaining separation and stabilising the emulsion.

For comparison, we also performed a separate set of simulations in which the polarisation field is treated as quasi-static. In this approximation, $\boldsymbol{p}$ is assumed to relax instantaneously to the configuration that minimises the free energy, namely

$$\frac{\delta F}{\delta \boldsymbol{p}} = \boldsymbol{0} \quad \Rightarrow \quad \boldsymbol{p} = -\frac{\varepsilon}{2}\boldsymbol{\nabla}\phi. \tag{3.26}$$

Under weak-flow conditions, where $\boldsymbol{v} \simeq \boldsymbol{0}$, we find no qualitative difference in the stability of the emulsion compared with fully dynamical model shown in figure 4(*b*). However, in the presence of a strong imposed shear, similar to that in figure 3(*c*), some quantitative and/or qualitative difference may emerge.

## 4. Conclusion

In this work, we have developed a continuum hydrodynamic model for binary-fluid–surfactant systems by systematically deriving both the microscopic and coarse-grained dynamics using Rayleigh's minimum energy dissipation principle. At the microscopic level, surfactant molecules are modelled as rigid dumbbells that undergo Brownian motion and exert forces and torques on the surrounding fluid due to their amphiphilic character, while the fluid is treated as a continuum field – resulting in a hybrid discrete–continuum formulation. By constructing an appropriate Rayleighian dissipation functional, we derived the overdamped stochastic equations governing the translational and rotational dynamics of individual surfactant molecules.

Upon coarse-graining these microscopic dynamics, we derived a closed set of continuum equations for the surfactant concentration field $c(r, t)$, polarisation field $\boldsymbol{p}(\boldsymbol{r}, t)$, binary fluid composition $\phi(\boldsymbol{r}, t)$ and fluid velocity $\boldsymbol{v}(\boldsymbol{r}, t)$. These equations follow consistently from a single mesoscopic free energy functional, ensuring thermodynamic consistency and preserving detailed balance at equilibrium.

Our model successfully captures key physical phenomena associated with surfactants, including their accumulation and alignment at interfaces, the reduction of surface tension, and the suppression of droplet coalescence in emulsions. These predictions were validated through a combination of perturbative analytical solutions and direct numerical simulations. Unlike previous approaches, our framework requires no *ad hoc* stabilising terms, as all interfacial effects and coupling mechanisms emerge naturally from the underlying variational formulation.

Beyond passive surfactants, our formalism is sufficiently general to accommodate additional microscopic ingredients. In particular, the Rayleighian framework and the polarisation dynamics can be readily extended to describe active particles at fluid–fluid interfaces, where self-propulsion, active forces and torques can modify the interfacial



https://doi.org/10.1017/jfm.2026.11248 Published online by Cambridge University Press

stresses (Saintillan & Shelley 2013). This opens the door to studying a broad class of non-equilibrium interfacial phenomena such as active emulsions, self-assembled interfacial monolayers and active Marangoni flows.

**Funding.** A.J.H. acknowledges EPSRC DTP Studentship No. 2739112. S.C. and E.T. acknowledges funding from EPSRC Grant No. EP/W027194/1. S.M.D. acknowledges London Mathematical Society Undergraduate Research Bursary URB-2024-40.

**Declaration of interests.** The authors report no conflict of interest.

**Use of generative AI.** The authors acknowledge the use of generative AI during the preparation of this manuscript for the purpose of improving grammar, enhancing clarity and supporting literature searches. All outputs produced by the tool were carefully checked and revised by the authors, who assume full responsibility for the integrity and accuracy of the published work.

## Appendix A. Alternative derivation of the coarse-grained free energy

In §§ 2.1 and 2.2, we derived the free energy functional using the Rayleigh dissipation functional. In this section, we show that one can also derive the free energy functional using direct thermodynamic arguments from Shannon entropy. The total free energy of the system is

$$F_{total}[\phi, c, \boldsymbol{p}] = F_{fluid}[\phi] + F_{surfactants}[\phi, c, \boldsymbol{p}], \tag{A1}$$

composed of $F_{fluid}[\phi]$, the free energy contribution from the binary fluid, and $F_{surfactants}[\phi, c, \boldsymbol{p}]$, the free energy contribution from the surfactant molecules. The fluid free energy is taken from standard Cahn–Hilliard theory (Lee *et al.* 2014), while the surfactant contributions are derived using the Helmholtz equation:

$$F_{surfactants}[\phi, c, \boldsymbol{p}] = U[\phi, c, \boldsymbol{p}] - T\,S[c, \boldsymbol{p}], \tag{A2}$$

where $U$ is the potential energy, $T$ is the temperature and $S$ is the Shannon entropy. The potential energy for the interaction between the molecules and the fluid can be calculated by summing the microscopic energy (second term in (2.8)) over all particles $i = 1, 2, \ldots N$, where $N$ is the total number of particles,

$$U[\phi, \{\boldsymbol{r}_i, \hat{\boldsymbol{e}}_i\}] = \chi\ell \sum_{i=1}^{N} \hat{\boldsymbol{e}}_i \cdot \nabla_i \phi(\boldsymbol{r}_i). \tag{A3}$$

Note that we have ignored higher order terms $\sim \ell^2$. Equation (A3) can then be coarse-grained straight into its continuum form:

$$U[\phi, c, \boldsymbol{p}] = \int_V (\chi\ell c\boldsymbol{p} \cdot \nabla\phi)\,\mathrm{d}V, \tag{A4}$$

by approximating

$$c(\boldsymbol{r}, t) \simeq \sum_{i=1}^{N} \delta(\boldsymbol{r} - \boldsymbol{r}_i) \quad \text{and} \quad c(\boldsymbol{r}, t)\boldsymbol{p}(\boldsymbol{r}, t) \simeq \sum_{i=1}^{N} \hat{\boldsymbol{e}}_i \delta(\boldsymbol{r} - \boldsymbol{r}_i). \tag{A5}$$

The entropic term can be derived using Shannon's information entropy expression together with our probability density $\psi(\boldsymbol{r}, \hat{\boldsymbol{e}}, t)$:

$$S[c, \boldsymbol{p}] = -k_B \int d^d r \int d^{d-1}\hat{e}\ \left[\psi \ln(\mathcal{N}\psi)\right]. \tag{A6}$$

Here, $\mathcal{N}$ is a constant ensuring the argument of the logarithm remains dimensionless. This expression can be simplified by representing $\psi(\boldsymbol{r}, \hat{\boldsymbol{e}}, t)$ as a spherical harmonics expansion



https://doi.org/10.1017/jfm.2026.11248 Published online by Cambridge University Press

(see Appendix B):

$$\psi = \frac{1}{S_d} c + \frac{d}{S_d} c\boldsymbol{p}\cdot\hat{\boldsymbol{e}}, \tag{A7}$$

where $S_d$ is the surface area of a $d$-dimensional unit sphere. Higher-order terms are assumed to be negligible. Substituting this into (A6) yields

$$S[c,\,\boldsymbol{p}] = -\frac{k_B}{S_d}\int d^d r \int d^{d-1}\hat{e}\,\left(c + dc\boldsymbol{p}\cdot\hat{\boldsymbol{e}}\right)\left[\ln\left(\frac{\mathcal{N}c}{S_d}\right) + \ln\left(1 + d\,\boldsymbol{p}\cdot\hat{\boldsymbol{e}}\right)\right]. \tag{A8}$$

Expanding the second logarithmic term for small $\boldsymbol{p}$ gives

$$S[c,\,\boldsymbol{p}] = -\frac{k_B}{S_d}\int d^d r \int d^{d-1}\hat{e}\left[c\ln\left(\frac{\mathcal{N}c}{S_d}\right)\left(1 + d\,\boldsymbol{p}\cdot\hat{\boldsymbol{e}}\right) + dc\boldsymbol{p}\cdot\hat{\boldsymbol{e}} + \frac{1}{2}d^2 c\left(\boldsymbol{p}\cdot\hat{\boldsymbol{e}}\right)^2\right]. \tag{A9}$$

Integrating with respect to $\hat{\boldsymbol{e}}$ and using the results from Appendix (B) give us the final expression for the entropic contribution from the surfactants:

$$S[c,\,\boldsymbol{p}] = -k_B\int d^d r\left[c\ln\left(\frac{\mathcal{N}}{S_d}c\right) + \frac{d}{2}c|\boldsymbol{p}|^2\right]\mathrm{d}V\,. \tag{A10}$$

Combining (A4) with this entropy contribution along with the free energy of the fluid $F_{fluid}[\phi]$ yields the coarse-grained free energy of (2.36).

## Appendix B. Moment-averaging the single-particle distribution function

We expand the distribution function $\psi(\boldsymbol{r},\hat{\boldsymbol{e}},t)$ in terms of spherical harmonics as follows:

$$\psi(\boldsymbol{r},\hat{\boldsymbol{e}},t) = A_0 c(\boldsymbol{r},t) + A_1 c(\boldsymbol{r},t)\boldsymbol{p}(\boldsymbol{r},t)\cdot\hat{\boldsymbol{e}} + \cdot s. \tag{B1}$$

We assume higher order harmonics to be small so we may set $A_n = 0$ for all $n \geqslant 2$. We are now left with two coefficients $A_0$ and $A_1$, which are yet to be determined. To find these coefficients, we need the following results:

$$\int \hat{e}_\alpha\,\mathrm{d}\Omega_d = 0, \tag{B2a}$$

$$\int \hat{e}_\alpha\hat{e}_\beta\,\mathrm{d}\Omega_d = \frac{S_d}{d}\delta_{\alpha\beta}, \tag{B2b}$$

$$\int \hat{e}_\alpha\hat{e}_\beta\hat{e}_\gamma\,\mathrm{d}\Omega_d = 0, \tag{B2c}$$

$$\int \hat{e}_\alpha\hat{e}_\beta\hat{e}_\gamma\hat{e}_\delta\,\mathrm{d}\Omega_d = \frac{S_d}{d(d+2)}\left(\delta_{\alpha\beta}\delta_{\gamma\delta} + \delta_{\alpha\gamma}\delta_{\beta\delta} + \delta_{\alpha\delta}\delta_{\beta\gamma}\right), \tag{B2d}$$

where $S_d$ is the surface area of the $d$-dimensional unit sphere. For example, $S_2 = 2\pi$ and $S_3 = 4\pi$. Now, to find $A_0$, we integrate (B1) over the solid angle $\Omega_d$ :

$$\underbrace{\int \psi\,\mathrm{d}\Omega_d}_{c} = A_0 c\underbrace{\int \mathrm{d}\Omega_d}_{S_d} + A_1 c p_\alpha\underbrace{\int \hat{e}_\alpha\,\mathrm{d}\Omega_d}_{0} \Rightarrow A_0 = \frac{1}{S_d}. \tag{B3}$$



https://doi.org/10.1017/jfm.2026.11248 Published online by Cambridge University Press

To find $A_1$, we multiply (B1) by $\hat{e}_\alpha$, then integrate over the solid angle $\Omega_d$:

$$\underbrace{\int \psi \hat{e}_\alpha \,\mathrm{d}\Omega_d}_{cp_\alpha} = \frac{1}{S_d} c \underbrace{\int \hat{e}_\alpha \,\mathrm{d}\Omega_d}_{0} + A_1 c p_\beta \underbrace{\int \hat{e}_\alpha \hat{e}_\beta \,\mathrm{d}\Omega_d}_{\frac{S_d}{d}\delta_{\alpha\beta}} \Rightarrow A_1 = \frac{d}{S_d}. \tag{B4}$$

Therefore, the truncated spherical expansion for $\psi$ can be written as

$$\psi(\boldsymbol{r}, \hat{\boldsymbol{e}}, t) = \frac{1}{S_d} c(\boldsymbol{r}, t) + \frac{d}{S_d} c(\boldsymbol{r}, t) \boldsymbol{p}(\boldsymbol{r}, t) \cdot \hat{\boldsymbol{e}}. \tag{B5}$$

We can use (B5) to find the angular averages $\langle \hat{e}_\alpha \hat{e}_\beta \rangle$, $\langle \hat{e}_\alpha \hat{e}_\beta \hat{e}_\gamma \rangle$ and so on. For instance, to find $\langle \hat{e}_\alpha \hat{e}_\beta \rangle$, we use the definition for average:

$$\langle \hat{e}_\alpha \hat{e}_\beta \rangle = \int \psi(\boldsymbol{r}, \hat{\boldsymbol{e}}, t) \hat{e}_\alpha \hat{e}_\beta \,\mathrm{d}\Omega_d, \tag{B6}$$

which gives

$$\langle \hat{e}_\alpha \hat{e}_\beta \rangle = c \frac{\delta_{\alpha\beta}}{d}, \tag{B7a}$$

$$\langle \hat{e}_\alpha \hat{e}_\beta \hat{e}_\gamma \rangle = \frac{c}{d+2} \left( p_\gamma \delta_{\alpha\beta} + p_\beta \delta_{\alpha\gamma} + p_\alpha \delta_{\beta\gamma} \right). \tag{B7b}$$

## Appendix C. Non-dimensionalisation

In this appendix, we use the bar notation to indicate non-dimensionalised quantities for clarity, however, in the main text, the reverse is true. In the following, we consider the dynamics of coupled surfactant–binary fluid systems in general $d$-dimension. In the simulation, we consider $d = 2$ mostly. To get the dimensionless form of the free energy, we introduce $\xi_I = \sqrt{2\kappa/\beta}$ as the unit of length and $k_B T$ as the unit of energy. Dividing (2.36) by $k_B T$ and rescaling space $\boldsymbol{r} = \xi_I \bar{\boldsymbol{r}}$, the free energy becomes (note that bars indicate dimensionless quantities)

$$\bar{F} = \frac{F}{k_B T} = \int \Bigg\{ -\frac{1}{2}\frac{\beta \xi_I^d}{k_B T}\phi^2 + \frac{1}{4}\frac{\beta \xi_I^d}{k_B T}\phi^4 + \frac{1}{2}\frac{\kappa \xi_I^{d-2}}{k_B T}|\bar{\nabla}\phi|^2 + \bar{c}\ln(\bar{c}) + \frac{d}{2}\bar{c}|\boldsymbol{p}|^2 + \frac{\chi \ell}{\xi_I k_B T}\bar{c}\boldsymbol{p}\cdot\bar{\nabla}\phi \Bigg\} d^d\bar{r} \tag{C1}$$

Now, we define the dimensionless parameters to be

$$\bar{\beta} = \frac{\beta \xi_I^d}{k_B T}, \quad \bar{\kappa} = \frac{\kappa \xi_I^{d-2}}{k_B T} = \frac{\bar{\beta}}{2} \quad \text{and} \quad \varepsilon = \frac{\chi \ell}{\xi_I k_B T}, \tag{C2}$$

so that the free energy becomes

$$\bar{F} = \int \left\{ -\frac{\bar{\beta}}{2}\phi^2 + \frac{\bar{\beta}}{4}\phi^4 + \frac{\bar{\beta}}{4}|\bar{\nabla}\phi|^2 + \bar{c}\ln(\bar{c}) + \frac{d}{2}\bar{c}|\boldsymbol{p}|^2 + \varepsilon \bar{c}\boldsymbol{p}\cdot\bar{\nabla}\phi \right\} d^d\bar{r}. \tag{C3}$$

Now, we introduce $\tau$ as the unit of time, so the equations of motion (2.40) become

$$\frac{\partial \phi}{\partial \bar{t}} + (\bar{\boldsymbol{v}}\cdot\bar{\nabla})\phi = \bar{M}\bar{\nabla}^2 \left[ -\bar{\beta}\phi + \bar{\beta}\phi^3 - \frac{\bar{\beta}}{2}\bar{\nabla}^2\phi - \varepsilon \bar{\nabla}\cdot(\bar{c}\boldsymbol{p}) \right], \tag{C4a}$$



https://doi.org/10.1017/jfm.2026.11248 Published online by Cambridge University Press

$$\frac{\partial \bar{c}}{\partial \bar{t}} + (\bar{\boldsymbol{v}} \cdot \bar{\boldsymbol{\nabla}})\bar{c} = \frac{1}{\bar{\gamma}_t}\bar{\nabla}^2 \bar{c} + \frac{1}{\bar{\gamma}_t}\bar{\boldsymbol{\nabla}} \cdot \left[\bar{c}\bar{\boldsymbol{\nabla}}\left(\frac{d}{2}|\boldsymbol{p}|^2 + \varepsilon \boldsymbol{p} \cdot \bar{\boldsymbol{\nabla}}\phi\right)\right], \tag{C4b}$$

$$\frac{\partial \boldsymbol{p}}{\partial \bar{t}} + (\bar{\boldsymbol{v}} \cdot \bar{\boldsymbol{\nabla}})\boldsymbol{p} = -\bar{\boldsymbol{\Omega}} \cdot \boldsymbol{p} - \frac{Bd}{d+2}\bar{\boldsymbol{D}} \cdot \boldsymbol{p} - \frac{d-1}{\mathrm{d}\bar{\gamma}_r}(d\boldsymbol{p} + \varepsilon \bar{\boldsymbol{\nabla}}\phi), \tag{C4c}$$

where we have introduced the dimensionless parameters

$$\bar{M} = \frac{Mk_BT\tau}{\xi_I^{d+2}}, \quad \frac{1}{\bar{\gamma}_t} = \frac{k_BT\tau}{\gamma_t \xi_I^2} \quad \text{and} \quad \frac{1}{\bar{\gamma}_r} = \frac{k_BT\tau}{\gamma_r}. \tag{C5}$$

The Stokes equation (2.41) becomes

$$0 = -\bar{\boldsymbol{\nabla}}\bar{P} + \bar{\eta}\bar{\nabla}^2\bar{\boldsymbol{v}} + \bar{\boldsymbol{f}} + \bar{\boldsymbol{\nabla}} \cdot \bar{\boldsymbol{\sigma}}, \tag{C6}$$

where $\bar{P} = \xi_I^d P/(k_BT)$ is the dimensionless pressure and $\bar{\eta} = \eta\xi_I^d/(\tau k_BT)$ is the dimensionless viscosity. Here, $\bar{\boldsymbol{f}}$ and $\bar{\boldsymbol{\sigma}}$ are the dimensionless force density and stress, respectively:

$$\bar{\boldsymbol{f}} = \frac{\xi_I^{d+1}}{k_BT}\boldsymbol{f} = -\phi\bar{\boldsymbol{\nabla}}\frac{\delta \bar{F}}{\delta \phi} - \bar{c}\bar{\boldsymbol{\nabla}}\frac{\delta \bar{F}}{\delta \bar{c}} - \boldsymbol{p} \cdot \left(\bar{\boldsymbol{\nabla}}\frac{\delta \bar{F}}{\delta \boldsymbol{p}}\right)^T, \tag{C7a}$$

$$\bar{\boldsymbol{\sigma}} = \frac{\xi_I^d}{k_BT}\boldsymbol{\sigma} = \frac{Bd}{2(d+2)}\left(\boldsymbol{p}\frac{\delta \bar{F}}{\delta \boldsymbol{p}} + \frac{\delta \bar{F}}{\delta \boldsymbol{p}}\boldsymbol{p}\right) - \frac{1}{2}\left(\boldsymbol{p}\frac{\delta \bar{F}}{\delta \boldsymbol{p}} - \frac{\delta \bar{F}}{\delta \boldsymbol{p}}\boldsymbol{p}\right). \tag{C7b}$$

## Appendix D. Numerical boundary conditions

In our two-dimensional simulation, the space $\boldsymbol{r} = (x, y)$ is discretised into $x = i\Delta x$ and $y = j\Delta y$, where $i = 0, 1, 2, \ldots N_x - 1$ and $j = 0, 1, 2, \ldots N_y - 1$. Here, $N_x$ and $N_y$ are the number of lattice points along the $x$- and $y$-axis, and $\Delta x$ and $\Delta y$ are the corresponding lattice spacing. The domain size is then $L_x = N_x\Delta x$ along $x$ and $L_y = N_y\Delta y$ along $y$. We also discretise the time $t$ into $t = n\Delta t$, where $n = 0, 1, 2, \ldots$. The hydrodynamic variables such as $\phi(\boldsymbol{r}, t)$, $c(\boldsymbol{r}, t)$, etc. are then discretised into $\phi(\boldsymbol{r}, t) \to \phi_{ij}^n$, and so on. The $\phi$-dynamics, (3.2*a*), can be discretised into

$$\phi_{ij}^{n+1} = \phi_{ij}^n - \Delta t\,(\boldsymbol{\nabla} \cdot \boldsymbol{J})_{ij}^n + \Delta t M\left(\nabla^2\mu\right)_{ij}^n, \tag{D1}$$

where $\boldsymbol{J} = \phi\boldsymbol{v}$ and $\mu = \delta F/\delta\phi = -\beta\phi + \beta\phi^3 - \beta\nabla^2\phi/2 - \varepsilon\boldsymbol{\nabla} \cdot (c\boldsymbol{p})$. Since $\int \phi(\boldsymbol{r}, t)\,\mathrm{d}^2 r$ is conserved, we need to ensure that the discretised $\phi_{ij}^n$ is also conserved, i.e.

$$\sum_{i=0}^{N_x-1}\sum_{j=0}^{N_y-1}\phi_{ij}^n = \text{constant for all } n \in \mathbb{Z}. \tag{D2}$$

To ensure this, we discretised $\boldsymbol{\nabla} \cdot \boldsymbol{J}$ and $\nabla^2\mu$ as follows:

$$(\boldsymbol{\nabla} \cdot \boldsymbol{J})_{ij}^n = \frac{J_{x,i+1,j}^n - J_{x,i-1,j}^n}{2\Delta x} + \frac{J_{y,i,j+1}^n - J_{y,i,j-1}^n}{2\Delta y}, \tag{D3a}$$

$$\left(\nabla^2\mu\right)_{ij}^n = \frac{\mu_{i+1,j}^n + \mu_{i,j}^n + \mu_{i-1,j}^n}{\Delta x^2} + \frac{\mu_{i,j+1}^n + \mu_{i,j}^n + \mu_{i,j-1}^n}{\Delta y^2}. \tag{D3b}$$



https://doi.org/10.1017/jfm.2026.11248 Published online by Cambridge University Press

We impose the periodic boundary conditions at $j = 0$ and $j = N_y - 1$ by having

$$\boldsymbol{J}^n_{i,0} = \boldsymbol{J}^n_{i,N_y-1}, \quad \phi^n_{i,0} = \phi^n_{i,N_y-1} \quad \text{and} \quad \mu^n_{i,0} = \mu^n_{i,N_y-1} \tag{D4}$$

for all $i$ and $n$. We impose the no-flux boundary conditions at $i = 0$ and $i = N_x - 1$ by having

$$J^n_{x,0,j} = -J^n_{x,1,j}, \quad J^n_{x,N_x-1,j} = -J^n_{x,N_x-2,j}, \tag{D5}$$

$$\phi^n_{0,j} = \phi^n_{1,j}, \quad \phi^n_{N_x-1,j} = \phi^n_{N_x-2,j}, \tag{D6}$$

$$\mu^n_{0,j} = \mu^n_{1,j} \quad \text{and} \quad \mu^n_{N_x-1,j} = \mu^n_{N_x-2,j} \tag{D7}$$

for all $j$ and $n$. Similar boundary conditions are also used for $c(\boldsymbol{r}, t)$ and $\boldsymbol{p}(\boldsymbol{r}, t)$, except the no-flux condition does not apply to $\boldsymbol{p}$.

## References


Ahluwalia, R. & Puri, S. 1996 Phase-ordering dynamics in binary mixtures with surfactants. *J. Phys.: Condens. Matter* **8** (3), 227.

Alexander, S. 1978 A lattice gas model for microemulsions. *J. Physique Lett.* **39** (1), 1–3.

Anisimov, M.A., Gorodetsky, E.E., Davydov, A.J. & Kurliandsky, A.S. 1992 Landau model for self-assembly and liquid crystal formation in surfactant solutions. *Liq. Cryst.* **11** (6), 941–947.

Benzi, R., Succi, S. & Vergassola, M. 1992 The lattice Boltzmann equation: theory and applications. *Phys. Rep.* **222** (3), 145–197.

Booty, M.R. & Siegel, M. 2010 A hybrid numerical method for interfacial fluid flow with soluble surfactant. *J. Comput. Phys.* **229** (10), 3864–3883.

Cates, M.E. & Tjhung, E. 2018 Theories of binary fluid mixtures: from phase-separation kinetics to active emulsions. *J. Fluid Mech.* **836**, P1.

Chan, C.K. & Liang, N.Y. 1990 Critical phenomena in an immiscible lattice-gas cellular automaton. *Europhys. Lett. (EPL)* **13** (6), 495–500.

Dai, B. & Leal, L.G. 2008 The mechanism of surfactant effects on drop coalescence. *Phys. Fluids* **20** (4), 040802.

Doi, M. 2011 Onsager's variational principle in soft matter. *J. Phys.: Condens. Matter* **23** (28), 284118.

Doi, M. 2013 *Soft Matter Physics*. OUP Oxford.

Doi, M. & Edwards, S.F. 1986 *The Theory of Polymer Dynamics*. Clarendon Press.

Erik Teigen, K., Song, P., Lowengrub, J. & Voigt, A. 2011 A diffuse-interface method for two-phase flows with soluble surfactants. *J. Comput. Phys.* **230** (2), 375–393.

Faria, B.F. & Vishnyakov, A.M. 2022 Simulation of surfactant adsorption at liquid–liquid interface: what we may expect from soft-core models? *J. Chem. Phys.* **157** (9), 094706.

Frisch, U., Hasslacher, B. & Pomeau, Y. 1986 Lattice-gas automata for the Navier–Stokes equation. *Phys. Rev. Lett.* **56**, 1505–1508.

Ganesan, S. 2015 Simulations of impinging droplets with surfactant-dependent dynamic contact angle. *J. Comput. Phys.* **301**, 178–200.

Gangula, S., Suen, S.-Y. & Conte, E.D. 2010 Analytical applications of admicelle and hemimicelle solid phase extraction of organic analytes. *Microchem. J.* **95** (1), 2–4.

Gilhøj, H., Laradji, M., Dammann, B., Jeppesen, C., Mouritsen, O.G., Toxvaerd, S. & Zuckermann, M.J. 1996 Effect of vacancies and surfactants on the dynamics of ordering processes in multi-component systems. *Math. Comput. Simulat.* **40** (3), 319–337.

Hardy, A.J., Daddi-Moussa-Ider, A. & Tjhung, E. 2024 Hybrid particle-phase field model and renormalized surface tension in dilute suspensions of nanoparticles. *Phys. Rev. E* **110**, 044606.

Harris, C.R., *et al.* 2020 Array programming with NumPy. *Nature* **585** (7825), 357–362.

Higuera, F.J., Succi, S. & Benzi, R. 1989 Lattice gas dynamics with enhanced collisions. *Europhys. Lett. (EPL)* **9** (4), 345–349.

Hoffmann, M., Wagner, C.S., Harnau, L. & Wittemann, A. 2009 3d brownian diffusion of submicron-sized particle clusters. *ACS Nano* **3** (10), 3326–3334.

Jaensson, N.O., Hulsen, M.A. & Anderson, P.D. 2017 On the use of a diffuse-interface model for the simulation of rigid particles in two-phase newtonian and viscoelastic fluids. *Comput. Fluids* **156**, 81–96.

Jeffery, G.B. 1922 The motion of ellipsoidal particles immersed in a viscous fluid. *Proc. R. Soc. Lond. Series A Contain. Papers Math. Phys. Charact.* **102** (715), 161–179.




https://doi.org/10.1017/jfm.2026.11248 Published online by Cambridge University Press

KALAM, S., ABU-KHAMSIN, S.A., KAMAL, M.S. & PATIL, S. 2021 Surfactant adsorption isotherms: a review. *ACS Omega* **6** (48), 32342–32348.

KAWAKATSU, T. & KAWASAKI, K. 1990 Hybrid models for the dynamics of an immiscible binary mixture with surfactant molecules. *Phys. A: Statist. Mech. Appl.* **167** (3), 690–735.

KAWASAKI, K. & KAWAKATSU, T. 1990 Continuum theory of an immiscible binary fluid mixture with a surfactant. *Phys. A: Statist. Mech. Appl.* **164** (3), 549–563.

KIAN FAR, E., GORAKIFARD, M. & FATTAHI, E. 2021 Multiphase phase-field lattice boltzmann method for simulation of soluble surfactants. *Symmetry* **13** (6), 1019.

KIM, J. 2006 Numerical simulations of phase separation dynamics in a water-oil-surfactant system. *J. Colloid Interface Sci.* **303** (1), 272–279.

KIM, S. & KARRILA, S.J. 2005 *Microhydrodynamics: Principles and Selected Applications*. Dover Publications.

KREBS, T., SCHROËN, K. & BOOM, R. 2012 Coalescence dynamics of surfactant-stabilized emulsions studied with microfluidics. *Soft Matt.* **8**, 10650–10657.

KRÜGER, T., KUSUMAATMAJA, H., KUZMIN, A., SHARDT, O., SILVA, G. & VIGGEN, E.M. 2017 *The Lattice Boltzmann Method: Principles and Practice*. Springer International Publishing.

LARADJI, M. & MOURITSEN, O.G. 2000 Elastic properties of surfactant monolayers at liquid–liquid interfaces: a molecular dynamics study. *J. Chem. Phys.* **112** (19), 8621–8630.

LEE, D., HUH, J.-Y., JEONG, D., SHIN, J., YUN, A. & KIM, J. 2014 Physical, mathematical, and numerical derivations of the Cahn–Hilliard equation. *Comput. Mater. Sci.* **81**, 216–225.

LIU, H. & ZHANG, Y. 2010 Phase-field modeling droplet dynamics with soluble surfactants. *J. Comput. Phys.* **229** (24), 9166–9187.

LOVE, P.J., NEKOVEE, M., COVENEY, P.V., CHIN, J., GONZÁLEZ-SEGREDO, N. & MARTIN, J.M.R. 2003 Simulations of amphiphilic fluids using mesoscale lattice-boltzmann and lattice-gas methods. *Comput. Phys. Commun.* **153** (3), 340–358.

MANIKANTAN, H. & SQUIRES, T.M. 2020 Surfactant dynamics: hidden variables controlling fluid flows. *J. Fluid Mech.* **892**, P1.

MARKOVICH, T., TJHUNG, E. & CATES, M.E. 2019 Chiral active matter: microscopic 'torque dipoles' have more than one hydrodynamic description. *New J. Phys.* **21** (11), 112001.

MELENKEVITZ, J. & JAVADPOUR, S.H. 1997 Phase separation dynamics in mixtures containing surfactants. *J. Chem. Phys.* **107** (2), 623–629.

MULQUEEN, M. & BLANKSCHTEIN, D. 2002 Theoretical and experimental investigation of the equilibrium oil–water interfacial tensions of solutions containing surfactant mixtures. *Langmuir* **18** (2), 365–376.

PELUSI, F., LULLI, M., SBRAGAGLIA, M. & BERNASCHI, M. 2022 Tlbfind: a thermal lattice boltzmann code for concentrated emulsions with finite-size droplets. *Comput. Phys. Commun.* **273**, 108259.

ROTHMAN, D.H. & KELLER, J.M. 1988 Immiscible cellular-automaton fluids. *J. Stat. Phys.* **52** (3-4), 1119–1127.

SAINTILLAN, D. & SHELLEY, M.J. 2013 Active suspensions and their nonlinear models. *C. R. Phys.* **14** (6), 497–517.

SANTOS, A.P. & PANAGIOTOPOULOS, A.Z. 2016 Determination of the critical micelle concentration in simulations of surfactant systems. *J. Chem. Phys.* **144** (4), 044709.

SHABAN, S.M., KANG, J. & KIM, D.-H. 2020 Surfactants: recent advances and their applications. *Compos. Commun.* **22**, 100537.

VAN DER SMAN, R.G.M. & VAN DER GRAAF, S. 2006 Diffuse interface model of surfactant adsorption onto flat and droplet interfaces. *Rheol. Acta* **46** (1), 3–11.

SOLIGO, G., ROCCON, A. & SOLDATI, A. 2019*a* Bre*a*kage, coalescence and size distribution of surfactant-laden droplets in turbulent flow. *J. Fluid Mech.* **881**, 244–282.

SOLIGO, G., ROCCON, A. & SOLDATI, A. 2019*b* Coalescence of surfactant-laden drops by phase field method. *J. Comput. Phys.* **376**, 1292–1311.

TADROS, T.F. 2005 *Applied Surfactants*. John Wiley and Sons, Ltd.

THEISSEN, O. & GOMPPER, G. 1999 Lattice-boltzmann study of spontaneous emulsification. *Eur. Phys. J. B - Condens. Matter Complex Syst.* **11** (1), 91–100.

TOUHAMI, Y., RANA, D., NEALE, G.H. & HORNOF, V. 2001 Study of polymer-surfactant interactions via surface tension measurements. *Colloid Polym. Sci.* **279** (3), 297–300.

WANG, L., HAGHMORADI, A., LIU, J., XI, S., HIRASAKI, G.J., MILLER, C.A. & CHAPMAN, W.G. 2017 Modeling micelle formation and interfacial properties with isaft classical density functional theory. *J. Chem. Phys.* **146** (12), 124705.

YAMASHITA, S., MATSUSHITA, S. & SUEKANE, T. 2024 Conservative transport model for surfactant on the interface based on the phase-field method. *J. Comput. Phys.* **516**, 113292.



https://doi.org/10.1017/jfm.2026.11248 Published online by Cambridge University Press

YANG, X. 2021 A novel fully-decoupled, second-order and energy stable numerical scheme of the conserved allen–cahn type flow-coupled binary surfactant model. *Comput. Method. Appl. Mech. Engng* **373**, 113502.

ZHU, G., KOU, J., YAO, J., LI, A. & SUN, S. 2020 A phase-field moving contact line model with soluble surfactants. *J. Comput. Phys.* **405**, 109170.

ZONG, Y., ZHANG, C., LIANG, H., WANG, L. & XU, J. 2020 Modeling surfactant-laden droplet dynamics by lattice boltzmann method. *Phys. Fluids* **32** (12), 122105.

https://doi.org/10.1017/jfm.2026.11248 Published online by Cambridge University Press